IONOSPHERIC RESPONSE TO SOLAR FLARES
USING AN IMPROVED VERSION OF SAMI2

THESIS

Joseph P. Reich III, Captain, USAF

AFIT/GAP/ENP/08-M08

DEPARTMENT OF THE AIR FORCE
AIR UNIVERSITY

AIR FORCE INSTITUTE OF TECHNOLOGY

Wright-Patterson Air Force Base, Ohio

AFIT/GAP/ENP/08-M08

Ionospheric Response to Solar Flares
Using an Improved Version of SAMI2

THESIS

Presented to the Faculty

Department of Engineering Physics

Graduate School of Engineering and Management

Air Force Institute of Technology

Air University

Air Education and Training Command

In Partial Fulfillment of the Requirements for the

Degree of Master of Science in Applied Physics
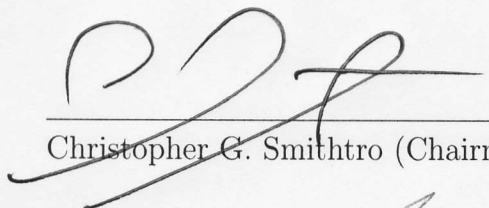
Joseph P. Reich III, AAS, B.S.

Captain, USAF

March 2008

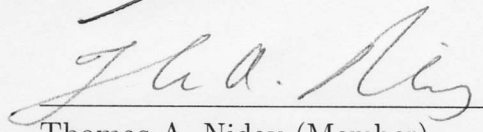# Ionospheric Response to Solar Flares Using an Improved Version of SAMI2

Joseph P. Reich III, AAS, B.S.

Captain, USAF

Approved:

_____
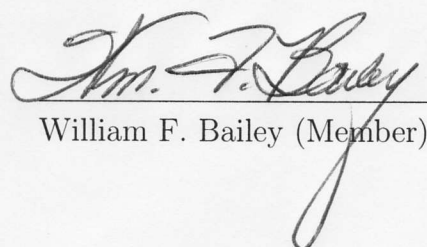Christopher G. Smithtro (Chairman)

19 Mar 2008
_____
Date

_____
Thomas A. Niday (Member)

19 Mar 2008
_____
Date

_____
William F. Bailey (Member)

19 Mar 2008
_____
Date

AFIT/GAP/ENP/08-M08

Abstract

Solar flares release energy, primarily at X-ray and EUV wavelengths, which is then absorbed mainly in Earth's ionosphere. This non-uniform absorption of energy alters the ionosphere's structure and can change the propagation of electromagnetic waves causing errors in GPS navigation, false radar echoes, and loss of High Frequency (HF) radio communications. Accurately modeling the ionospheric response to flares is the first step in predicting, and then mitigating, their effects. Accurately modeling these effects requires solar irradiance at a high cadence, to capture the flare, which may only last minutes, as well as treatment of the effects of photoelectrons. Sami2 is Another Model of the Ionosphere (SAMI2) is a two-dimensional ionospheric model. In its standard form, it is unsuitable for studying solar flare effects because it relies on a daily proxy to specify the solar irradiance. The model was successfully modified to include: secondary ionization of photoelectrons as well as high-cadence solar irradiance from the Flare Irradiance Spectral Model (FISM), and a new photoelectron heating parameterization. The modified SAMI2 was successfully used to model the ionospheric response to the X17 solar flare of 28 October, 2003. Long-lived enhancements in the total electron content (TEC) were observed as was an asymmetric increase in electron temperature due to increased photoelectron heating. Increases in electron temperature of more than 500 K were observed in the mid-latitudes of the Northern Hemisphere without a corresponding increase in the Southern Hemisphere.

Acknowledgements

I would like to offer sincere thanks to my research advisor. This work is, in large part due to his unending patience and encouragement. I would also like to recognize my family. Their patience and understanding, while not always fully appreciated, was no less valuable. Dr. Joe Huba provided several FORTRAN routines for calculating H_mF_2, N_mF_2, and TEC. His advice and encouragement was greatly appreciated.

Joseph P. Reich III

Table of Contents

List of Figures

viii

List of Tables

x

Ionospheric Response to Solar Flares
Using an Improved Version of SAMI2

I. Introduction

1.1 Motivation

As the Air Force enters the 21st century, its exploitation of the electromagnetic (E-M) spectrum continues to grow. Long-distance communications, radar, command and control of unmanned aerial vehicles (UAVs), intelligence gathering, and navigation using the Global Positioning System (GPS) must all pass through or reflect off the region of the atmosphere called the ionosphere. Changes to the structure of the ionosphere due to solar flares can alter or prevent the propagation of E-M waves causing errors in single-frequency GPS, over-the-horizon radar, and High Frequency (HF) radio communications from D and E region absorption of radio waves. In order to anticipate and mitigate the effects of solar flares on Air Force systems, the response of the ionosphere must first be modeled and characterized.

During a solar flare, the solar output shortward of 200 nm can vary by several orders of magnitude, on time scales ranging from seconds to tens of minutes. This energy is preferentially absorbed at low altitude in the atmosphere, between 60 and 300 km, increasing electron (and ion) density and electron temperature, which are further modified by the neutral winds, electric fields, and the Earth's magnetic field [*Schunk and Nagy*, 2000].

1.2 Problem Statement

Most ionospheric models are not adequate for the study of solar flares, which occur on time-scales of minutes to hours. The main limitation is insufficient temporal resolution of the solar irradiance. Many current models use the Solar Extreme Ultraviolet Flux Model for Aeronomic Calculations (EUVAC) [*Richards et al.*, 1994] to specify the solar irradiance. This model uses the 10.7 cm solar flux (10^{-22}W m^{-2} Hz^{-1}), a daily measurement, as a proxy for the solar irradiance. This yields a solar spectrum which is constant over the course of a day, only varying as a function of solar zenith angle (χ) and optical depth (*tau*). A solar irradiance spectrum which varies on the order of 60 seconds, or less, is necessary to capture the detail of a solar flare, which begins, peaks, and decays over a period of a few minutes to an hour. Over the past decade, new satellite measurements of solar irradiance have allowed the development of a more accurate model of solar flare irradiance at a cadence sufficient for modeling the ionospheric response to a flare. Additionally, the processing power of personal computers has advanced to the point where running a research-quality ionospheric model no longer requires a large investment in hardware.

This research takes an ionospheric model from the Naval Research Laboratory (NRL), Sami2 is Another Model of the Ionosphere (SAMI2) [*Huba et al.*, 2000], and makes several modifications to it. First, the model code is rewritten to use the 22-bin solar irradiance scheme from *Solomon and Qian* [2005]. This allows the inclusion, by the use of multiplicative factors, of additional ionization due to dissociative and photoelectron ionization. Next, the photoelectron heating parameterization is re-

2

placed with a new one, which responds to the increased short-wavelength irradiance during a flare. Finally, further modification enables the model to move from using EUVAC irradiance to the high-cadence irradiance of the Flare Irradiance Spectral Model (FISM) [*Chamberlin et al.*, 2007]. Once these changes are in place the model is used to investigate the ionospheric response to a flare.

1.3 Previous Work

Studies of the ionospheric response to solar flares have been conducted by several researchers, however, most focus on the largest (and rarest) events. This bias is perfectly reasonable since these large events provide the least ambiguous effects, and this approach will be taken here. The ionosphere occupies a region of the atmosphere that is difficult to measure, either in-situ or remotely. It is located too high for balloon-borne instruments and the atmospheric density is too high for spacecraft to survive for long, especially below 200 km. Although dual-frequency GPS can be used to measure electron density, this is an integrated measurement which yields no information about variations with height. On the other hand, both incoherent scatter radar and the ionospheric sounder (ionosonde) can probe the ionosphere from the ground, yielding information about electron density and temperature; however, the former depends upon concurrence of data campaigns and flares , and the latter is often hampered by D and E region absorption during a strong flare. The consequence is that relatively few examples exist of the modeled response to a flare being compared to real data.

Two researchers have compared the ionospheric response to flares using ionosonde data. *Smithtro et al.* [2005] and *Parsons* [2006] both investigated the ionospheric response to flares with the peak flux from $10^{-5} - 10^{-4}$ W/m^2 (GOES M–X1 class) using the 1-D Time-Dependent Ionospheric Model (TDIM), developed at Utah State University. In order to specify the flare irradiance *Parsons* [2006] used FISM [*Chamberlin et al.*, 2007] in place of the EUVAC [*Richards et al.*, 1994]. The Global Airglow (GLOW) model [*Parsons*, 2006] was used to calculate photoelectron ionization and heating rates. *Smithtro et al.* [2005] used scaling factors with data from the Solar EUV Experiment (SEE) aboard the NASA Thermosphere, Ionosphere, Mesosphere, Energetics, and Dynamics (TIMED) satellite instead of FISM for the irradiance and used a heating factor based on the GOES X-ray flux to drive the electron volume heating rate. The results of these two papers were contradictory, although not conclusive. Smithtro was able to recreate, and pose a reasonable theory to explain, a decrease in the density at the F$_2$ peak (N_mF_2), and simultaneous increase in total electron content (TEC), just following the flare peak, where one TEC unit (TECU $= 10^{16}$ m^{-2}. Parsons was not able to recreate this *flare notch*, but showed the more conventional increase in TEC and increase in N_mF_2.

Several studies have been published using SAMI2 and SAMI3 by its principal designers, *Huba et al.* [2000, 2002, 2003, 2005], including one on the effects of the Bastille Day solar flare of July 14, 2000. *Huba et al.* [2005] used SAMI3, a 3-dimensional version of SAMI2 which allows zonal transport of plasma. Instead of using EUVAC, they generated the irradiance spectrum via a time-dependent hydrodynamic code [*Mariska*

et al., 1989] with the UV and EUV wavelengths limited by the data from the Transition Region and Coronal Explorer (TRACE) satellite [*Huba et al.*, 2005]. Results were consistent with previous results from *Tsurutani et al.* [2005] and *Meier et al.* [2002] in TEC increases at and around the sub-solar point. They also noted that at the sub-solar point, H_mF_2 decreased by nearly 100 km and N_mF_2 increased by around 10% [*Huba et al.*, 2005]. The authors pointed out two important differences in the model output when compared to the Global Positioning Satellite (GPS) data. First, the model predicted a slower TEC rise time than was actually observed. The authors allow that there may be two causes for this: SAMI3, like SAMI2 doesn't include ionization by photoelectrons, and the temporal resolution of the modeled irradiance (5 min) may be too slow [*Huba et al.*, 2005]. Second, they found a persistence in the TEC enhancement not reflected in the GPS data. They suggested that this could be due to day-to-day spatial variations of the equatorial anomaly which are not included in the model [*Huba et al.*, 2005].

Meier et al. [2002] used SAMI2 to investigate the Bastille Day flare of July 14, 2000, but replaced EUVAC with a more suitable irradiance model. A modified version of the Naval Research Laboratory Extreme Ultraviolet model (NRLEUV) [*Warren et al.*, 2001; *Lean et al.*, 2003] was used in place of EUVAC, using the Atmospheric Ultraviolet Radiance Integrated Code (AURIC) used to calculate energy deposition rates, photoelectron fluxes, excitation rates, and column emission rates [*Meier et al.*, 2002]. They found an asymmetric response between the Northern and Southern Hemispheres, with a 40% increase in N_mF_2 in the Northern Hemisphere

versus a nearly 30% increase in the Southern Hemisphere, although no observations were available to corroborate the model results. Their results were, however, consistent with the work of *Tsurutani et al.* [2005], who, for the same flare, found that the flare subsolar point was the point of greatest increase in TEC, about 29 TECU above the preflare level. *Tsuritani's* study focused on an examination of the October 28, 2003 solar flare, which was one a several strong flares produced from late October through early November. He concluded that the October 28 flare produced a strong Extreme Ultraviolet (EUV) enhancement in addition to the more classic X-ray peak. This difference explained a long-lived (three hours) increase in the TEC that was not consistent with ionization from a large flare due to X-rays alone [*Tsurutani et al.*, 2005]. The enhancement they found is consistent with the results of this research effort, which is discussed in greater detail in Section 4.4.

II. Background

THIS chapter covers the principles necessary to understand the challenges associated with ionospheric modeling as it applies to the the study of solar flares. First, the chapter will briefly describe the ionosphere and its structure, followed by discussions of ionospheric modeling and the SAMI2 model. Next, a primer on solar flares and the utility of the FISM model over other models as the source for solar irradiance. Finally, an overview of photoelectrons and electron heating will cap the chapter.

2.1   The Ionosphere

The ionosphere is the region of the Earth's atmosphere consisting of *weakly* to *partially* ionized plasma. This region occupies the atmosphere from roughly 60 - 1000 km; however, the upper boundary can range between 600 - 1600 km [*Schunk and Nagy*, 2000]. A weakly ionized plasma is one in which collisions with neutral particles dominate. Ion-ion and ion-electron collisions can, therefore, be neglected in the momentum equation. In a partially ionized plasma, collisions between neutral constituents and charged particles must be accounted for and in a fully ionized plasma, such as that of the protonosphere, the neutral density is low enough that collisions between neutral atoms and charged particles can be ignored [*Schunk and Nagy*, 2000]. The terrestrial ionosphere is divided into four regions; in order of ascending altitude they are the D, E, F_1, and F_2 regions. The different regions are identified by relative maxima and are primarily distinguishable by electron density, production and loss

mechanisms, and persistence in response to diurnal changes in solar ionizing radiation. The D region, existing from 60 - 100 km, is composed largely of neutral gas with a small ionized component of molecular ions. Therefore, it is weakly ionized and collisions with ions can be ignored. Due to its high neutral density, chemical processes dominate the evolution of plasma in this region. When photochemistry dominates, the transport term in the ion continuity equation can be dropped yielding:

$$\frac{\partial n_s}{\partial t} = P_s - L_s \tag{2.1}$$

where P_s and L_s are production and loss mechanisms for each ion species and n_s is the density in cm^{-3}. Production terms include photoionization, photoelectron ionization and chemistry, while the main loss process is chemistry via recombination. Modeling the D region requires specialized models, owing to its complicated chemistry. This region plays a key role in the absorption of HF-radio signals, especially very low frequency (VLF) signals used in military communications; however, the D region is not treated by SAMI2 and is therefore, not discussed further.

The E region is found between 100 - 150 km where the neutral concentration ranges from 10^{13} cm^{-3} to 10^{11} cm^{-3} compared to ion concentrations on the order of 10^4 cm^{-3} to 10^5 cm^{-3}. Collisions with neutral species cannot be ignored; therefore, like the D region, it is weakly ionized. Here, NO$^+$ and O$_2^+$ are the dominant ions, and to a small extent, N$_2^+$. Production and loss mechanisms include photoionization by extreme ultraviolet (EUV) radiation shortward of 102 nm, ion-neutral chemical

reactions, and recombination. Since photochemistry dominates in this region too, ion transport can be neglected when calculating the electron density; however, it is included in SAMI2. Although the ion concentration in the E region generally decreases at nighttime, it is often maintained to some extent due to the presence of long-lasting metallic ions from meteor ablation, and ionization from starlight. Above the E region it is no longer possible to consider dropping transport from the momentum equation.

The F_1 and F_2 regions occupy the atmosphere from $150 - 250$ km, and 250 to ~ 700 km, respectively. The two regions are often difficult to distinguish, but at night the F_1 region decays leaving a valley between the F_2 and E regions. Unlike the lower ionosphere, where molecular ions are prevalent, in the F_2 region ionized atomic oxygen (O^+) is the most common ion, followed distantly by atomic nitrogen. The peak of the F_2 region occurs near 300 km; the region above 300 km is called the *topside* ionosphere. Although 1000 km was stated before as the upper limit for the ionosphere, it is better defined as the point where O^+ is overtaken by H^+ as the dominant ion. This point varies by latitude and the level of solar activity, but is generally between 600 and 1600 km [*Schunk and Nagy*, 2000]. The plasma concentration is roughly $10^5 - 10^6$ cm^{-3}, while the neutral concentration is $\simeq 10^8$ cm^{-3}. Collisions with both neutrals and ions must be considered, thus the region is partially ionized. While in the lower ionosphere it is possible to neglect transport in the continuity and momentum equations, it is not possible in the F_2 region. The ion concentration arises from a balance between production, loss, and transport. The continuity equation, shown

9

previously, is given below with the ion transport term intact:

$$\frac{\partial n_s}{\partial t} \; + \; \vec{\nabla} \cdot (n_s \vec{u}_s) \; = \; P_s - L_s \tag{2.2}$$

where the production and loss terms, P_s and L_s, are as in Equation 2.1, and $\vec{\nabla} \cdot (n_s \vec{u}_s)$ is the transport term of the total derivative. O^+ is created primarily through photoionization of atomic oxygen by wavelengths shorter than 91 nm; however, it is mainly lost through charge exchange reactions with N_2 and O_2. Unlike the F_1 region, the F_2 layer is maintained at night. There are two reasons for this. First, at the height of the F_2 layer the atmospheric density is too low for chemistry to act effectively so recombination works slowly. Second, as the O^+ density decreases, downward flowing H^+ from the plasmasphere helps maintain the region through charge exchange with neutral O [*Schunk and Nagy*, 2000].

The plasmasphere, or the protonosphere, is the region from the topside ionosphere, out to several thousand kilometers, that is dominated by H^+ and He^+. Like O, H is readily ionized by radiation shorter than 91 nm, although most H^+ is actually generated via charge exchange with O^+. Regardless of the mechanism, the resulting ions diffuse upward, constrained to flow along Earth's magnetic field, reaching heights of several thousand kilometers. The H^+ ions are relatively cold, less than 1 eV, and as a result the plasmasphere motion is characterized by co-rotation with the Earth, rather than the drift motion associated with the higher energy particles of Earth's ring current.

2.2   Ionospheric Modeling

Given the importance of space weather to communications and navigation, such as D region absorption of radio waves, and anomalous propagation due to variations in electron density, it is not surprising that ionospheric modeling is an area of intensive investigation. Of particular importance is the response of the ionosphere to the increased EUV and X-ray flux from solar flares, which can affect the entire sunlit hemisphere. In order to realistically model this response, an accurate model must be mated to an accurate solar spectrum.

Any model is an exercise in balancing computational cost with accuracy. Computational cost determines whether it requires a 120-processor mainframe, or whether it will run on a laptop. Accuracy is not an easy term to define, especially when it may take years of evaluating a model to identify its strengths and weaknesses. This is true of meteorological models which have comparatively easy access to verifying data, but doubly so of ionospheric models whose domain is largely inaccessible from direct measurement. At any rate, cost and accuracy are in direct competition. The most rigorous models use the most comprehensive physics (fewest parameterizations), and have a global (3-D) domain. Most models make use of parameterizations to speed computation, especially in areas where the added cost of a full-physics solution does not lead to significantly better results. This cost savings can be multiplied again if the domain is reduced from three to two, or one, dimension.

Accurate solar flare irradiance is an area that has seen recent advancements such as FISM [*Chamberlin*, 2005; *Chamberlin et al.*, 2007]. Irradiance models frequently use proxies in order to specify the solar output. Rather than try and measure the flare itself, which is difficult to measure accurately across the full X-ray to EUV spectrum, the major irradiance models use some, more easily measured, index to modify a baseline spectrum. These include the aforementioned FISM and EUVAC models, as well as the Hinteregger EUV81 (HFG) model [*Hinteregger et al.*, 1981] and SOLAR2000 [*Tobiska*, 2004] model. The NRLEUV, rather than being an empirical model, is physics-based and generates the flare spectrum by modeling a collection of coronal flux tubes, each with its own temperature and characteristic spectrum.

In order to properly model the ionosphere, the following non-inclusive list must be considered: direct photoionization and secondary ionization by photoelectrons, chemistry, plasma dynamics, the neutral atmosphere, and both electric and magnetic fields. The continuity, momentum, and temperature equations describe the evolution of the plasma, but can be simplified. Being a fluid, the plasma can move, therefore transport of must also be considered along and perpendicular to the Earth's magnetic field.

Models are frequently grouped into three types, low-latitude, mid-latitude, and high latitude [*Huba et al.*, 2000]. Since each regime presents its own set of unique challenges, one model rarely excels in all regions. Within the different latitudinal regimes, models may span 1, 2, or even 3 dimensions. The use of parameterizations can ease some of the computational cost of a model and there are two that are common to

many models. The Mass Spectrometer Incoherent Scatter (MSIS) [*Picone et al.*, 2002] and the Horizontal Wind Model (HWM) [*Hedin*, 1991] specify the neutral atmospheric density and neutral winds, respectively. The use of these models greatly shortens the run time of a model by providing realistic values without much overhead.

2.3 SAMI2

Sami2 is Another Model of the Ionosphere (SAMI2) is a 2-D (latitude and altitude) ionospheric model developed by the Naval Research Laboratory (NRL) [*Huba et al.*, 2000]. It models the mid and low-latitude ionosphere, including the geomagnetic equator, along a hemispheric grid from $90 - 20,000$ km. It was chosen for this research because it is freely available for modification from NRL, and the 2-D nature of the model allows more realistic evolution of the plasma than a 1-D model.

SAMI2 models the evolution of plasma along an inter-hemispheric magnetic flux tube, solving the continuity and momentum equations for 7 ion species: H^+, He^+, N^+, O^+, NO^+ and N_2^+, and O_2^+. Chemistry is handled via twenty-one chemical processes, including recombination. Temperatures are calculated for electrons and three ions O^+, H^+, and He^+. The model also includes $\mathbf{E} \times \mathbf{B}$ drift of the plasma using either of two electric field models. One is a simple sinusoidal model, the other is from *Scherliess and Fejer* [1999]. This allows the plasma to drift horizontally in the mid-latitudes and vertically near the dip equator where the magnetic field lines are nearly horizontal.

Although the model calculates the continuity and momentum equations directly, it makes use of several important parameterizations. First, EUVAC is used to specify

the daytime solar photon flux. EUVAC uses 37 wavelength bins based on a reference flux scaled by the daily $F_{10.7}$ index, and an 81-day center-weighted average of the index. Next, the neutral atmosphere and winds are calculated using the MSISE-00 and HWM93 empirical models. Finally, photoelectron heating is parameterized using a method from *Swartz and Nisbet* [1972].

The plasma is modeled using a non-orthogonal Eulerian grid, shown in Figure 2.1. The latitudinal extent of the domain is a function of the field line geometry and the height, above the geomagnetic equator of the highest field line. In this case, the altitude of the maximum field line is 7000 km, which yields a minimum and maximum latitude of 38° S and 52° N, respectively. Every fifth field line is plotted to illustrate the geometry, although the model utilized 228 field lines. The density of the field lines, and gridpoints, increases with decreasing altitude to increase low-altitude resolution. This can be adjusted in the model to equalize the spacing, but this was left at the default setting for this research. As the field lines move farther from the equator, they become more vertical. This adversely affects the low-altitude spatial resolution of the model, and the only remedy is to increase the number of field lines. This increases the model run time to unacceptable levels, taking roughly 12 hours to run a 48-hour simulation. The domain, with contoured data, is shown in Figure 2.2. Electron density (n_e) in cm^{-3} is plotted for 28 October, 2003 at 1110 UT using the model in its original configuration. The plot altitude has been decreased in order to show the low-altitude detail. The model ran for 36 hours, with the first 24 hours used

14
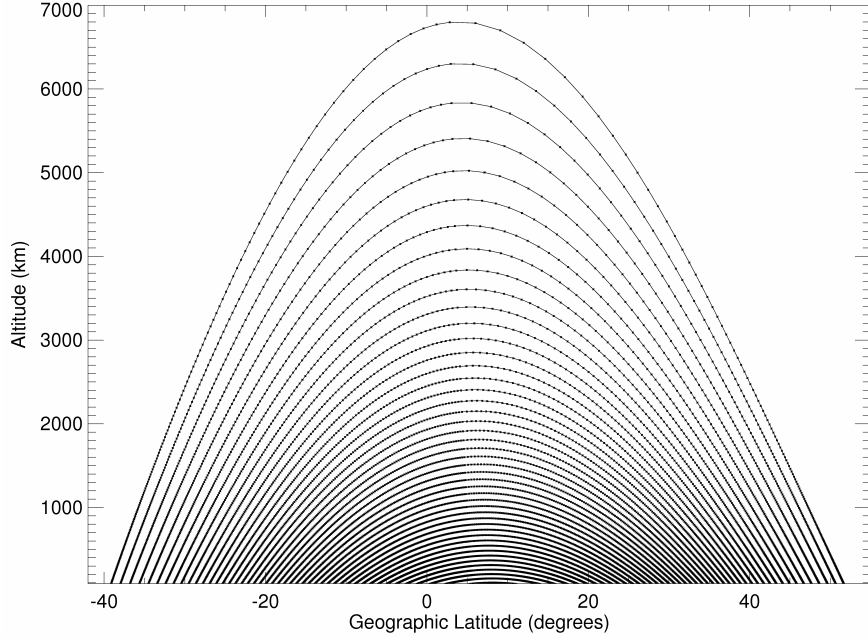
Figure 2.1.   The SAMI2 domain for 15° E with the altitude of the maximum field line (rmax) equal to 7000 km. The lowest field line (rmin) is 150 km. Every fifth field line is plotted to clearly show the geometry of the grid, which is comprised of 228 field lines and 301 grid points per field line.

to clear any transients from the system, then data is output every 15 minutes for the final 12 hours.

The plot shows a density maximum on each side of the geomagnetic equator. This is consistent with the *equatorial anomaly*, a sub-tropical electron density enhancement caused by $\mathbf{E} \times \mathbf{B}$ drift of plasma at the geomagnetic equator. The plasma lifts at the equator and creates a fountain-like effect as the as it spreads out and descends under the influence of gravity. The asymmetry of the density maxima, called the winter anomaly, is due to differences in the chemistry of the summer and winter hemispheres. Both these effects are further modified by the neutral winds, which can push the plasma up or down the field lines.

15
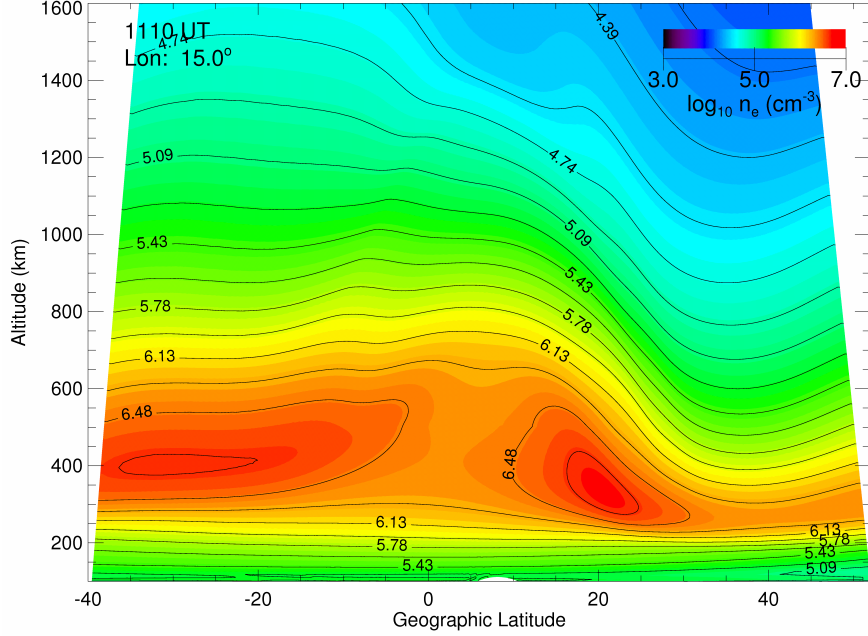
Figure 2.2.   SAMI2 electron density (n_e) in cm^{-3} s^{-1} on 28 October, 2003, 1110 UT at 15° E. Solar conditions are $F10.7 = 270.9$ and $\langle F10.7 \rangle = 188$. The domain is as in Figure 2.1, plotted in order to show low-altitude detail.

2.4   Solar Irradiance

The ionosphere is formed through absorption of incoming solar radiation with wavelengths shorter than 200 nm. At these wavelengths, photons possess sufficient energy to dissociate, excite, or ionize neutral particles. An example below shows the ionization of diatomic oxygen (O_2) by a photon ($h\nu$) with a wavelength shorter than 102.8 nm:

$$O_2 + h\nu \rightarrow O_2^+ + e \tag{2.3}$$

where e is the free electron, and $h\nu$, is the energy of the photon, which must exceed the ionization threshold of the neutral. In this case the minimum energy required to ionize O_2 is 12.06 eV.

16

Before the space age, this energy, comprising a small, but significant portion of the solar spectrum, was missed, since it does not reach below the height of the D region. By the early 1950's, the extreme ultraviolet and shorter wavelength spectra had been measured via rocket-borne sensors, and their importance to the ionosphere was firmly established [*Banks and Kockarts*, 1973]. The arrival of satellite-based measurements with their long residence, we could more completely measure the solar spectrum, and track its variability over the solar cycle. Figure 2.3 illustrates the variability of the extreme ultraviolet (EUV) down to 10 nm, as well as the lack of variation above 200 nm. At wavelengths shorter than 105 nm, the solar flux can increase by more than 125% during active periods, while the flux at longer wavelengths changes by less than 0.1%. While the vast majority of the Sun's output from visible light to radio waves come from the 5770 K photosphere, the much hotter (10^5–10^6 K), but much less dense chromosphere and corona, are responsible for the EUV and X-ray portions of the solar spectrum. During active periods, the short-wavelength emission is enhanced by intense bursts of energy called solar flares.

2.5   Solar Flares

A solar flare is a short-duration, localized brightening of the Sun's chromosphere and/or lower corona. These explosive bursts of energy occur on timescales ranging from seconds to minutes, making observation difficult until the advent of space-borne instruments. Space-based platforms can persist for years, even decades, tracking the Sun over the course of an entire solar cycle, and maintain nearly constant vigilance.
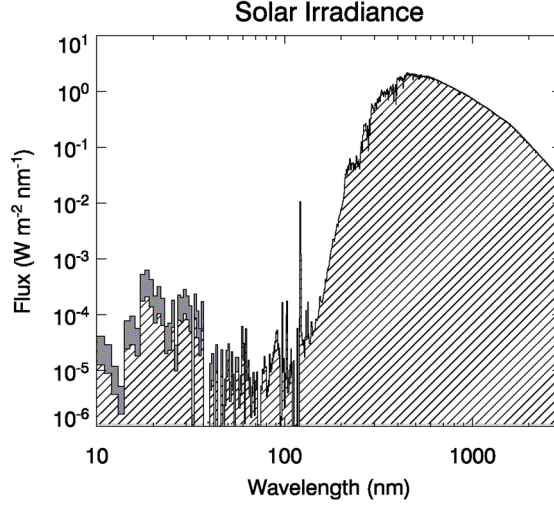
Figure 2.3.   Variability of the solar spectrum. The dark shaded region shows the change from periods of low solar activity to active periods.

These instruments also orbit at altitudes where absorption is minimal. This is especially important for accurate measurement of solar X-rays.

Theories abound as to the exact cause of solar flares, however nearly all involve the rapid conversion of magnetic energy to particle acceleration by a process called *magnetic reconnection. Aschwanden* [2004] offers a comprehensive treatment on the subject, which is too complex to fully explore here. Figure 2.4 shows the enhancement in ultraviolet (UV), and shorter wavelengths, above the quiet sun level for both an active Sun and a strong solar flare. At the soft X-ray (SXR), or X-ray ultraviolet (XUV) wavelengths, those from $0.1-10$ nm, the increase can be up to several orders of magnitude, while in the UV it is more modest. In the hard X-ray (HXR) range, from $10^{-3}-10^{-1}$ nm, the increase can be five orders of magnitude.

Solar flares are classified by their peak flux, in W/m^2 from $0.1-0.8$ nm (SXR region), as measured by the X-ray instrument onboard the GOES class of weather
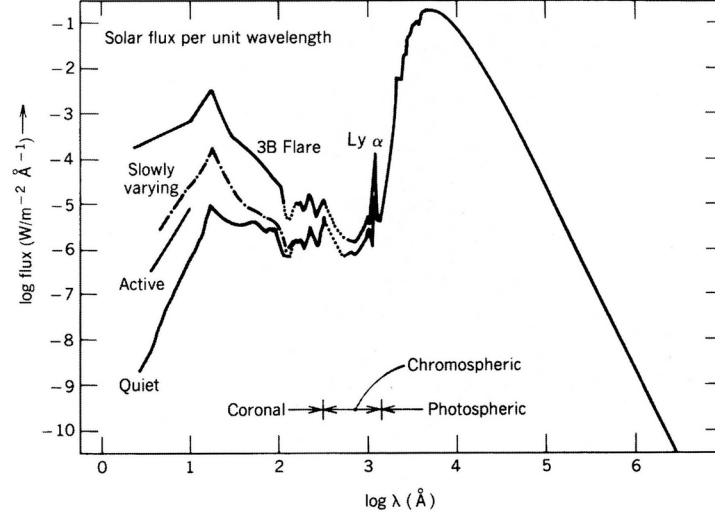
Figure 2.4.   Enhancement of the solar spectrum during a large solar flare. This demonstrates the order of magnitude changes in the X-ray range while the visible and longer wavelengths remain unchanged. Adapted from [*Foukal*, 2004].

satellites. Table 2.1 shows the current system used to classify solar flares, based on the peak flux. Photons in this energy range are caused by electrons accelerated to relativistic speeds (0.2–0.5 c) in the solar corona [*Aschwanden*, 2004]. These relativistic particles then loss their energy via *bremsstrahlung*, or braking, collisions with atomic nuclei in the transition region and chromosphere. The plot in Figure 2.5 shows the temporal evolution of a flare with idealized precursor, impulsive, and gradual phases. The precursor stage occurs just a few minutes before the impulsive phase, from 0 - 4 min, and is mainly in the SXR and XUV ranges. The impulsive phase begins and ends within just a minute or two and is measurable in all but the Hα and SXR where it is masked by the gradual phase. This phase is also seen in the microwave region and in the 100 - 300 MHz as a Type III radio burst. The gradual phase shows a much longer rise and fall time and is not easily seen in the HXR band, or in the radio frequencies. The bottom trace shows the T + 25 min arrival, at 1 AU, of energetic

19

protons and electrons. Our understanding of solar flare evolution has been pieced together over the past two decades and has benefited greatly from the additional data provided by satellite observations. A number of satellites are capable of imaging solar

Table 2.1.   Solar flare classification based on measured flux in W m^{-2} between 0.1 and 0.8 nm from the GOES satellite. An X1.7 flare = 1.7×10^{-4} W m^{-2}.

Classification	Peak Flux 0.1 - 0.8 nm (W m^{-2})
X	1×10^{-4}
M	1×10^{-5}
C	1×10^{-6}
B	1×10^{-7}
A	1×10^{-8}

flares at frequencies ranging in X-ray, and longer, wavelengths. The (Rueven) Ramaty High Energy Solar Spectroscopic Imager (RHESSI), and the Yohkoh Soft X-ray Telescope (SXT) are used to measure X-rays, while the Solar and Heliospheric Observatory (SOHO), and Transition Region And Coronal Explorer (TRACE) satellites are both optimized for the EUV range. The availability of new measurements of solar irradiance, and the observation at many wavelengths of solar flares, has enabled the creation of FISM model.
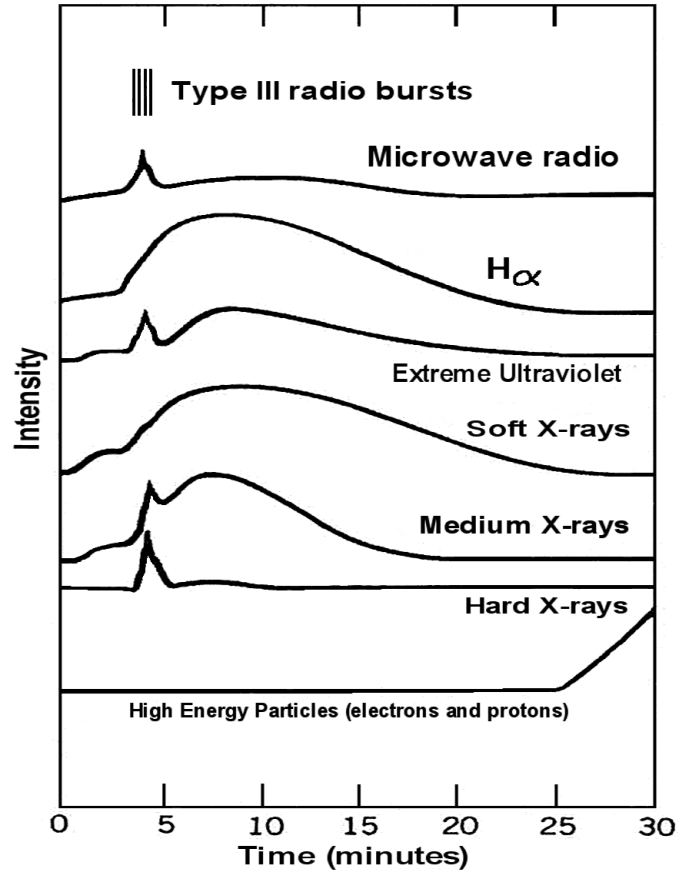
Figure 2.5. Temporal evolution of a solar flare showing the precursor, impulsive and gradual phases in various emission ranges. Adapted from *Foukal* [2004].

21

2.6 FISM

The Flare Irradiance Spectral Model (FISM), developed by *Chamberlin* [2005], is an empirical model of solar irradiance that produces a spectrum from X-ray to vacuum ultraviolet (VUV) wavelengths $(0.5 - 192.5$ nm) at 1 nm resolution, with a temporal resolution of 60 seconds [*Chamberlin et al.*, 2007]. Data from several platforms were used to construct a reference spectrum that is then increased based on daily, and higher cadence proxies, to model both flare, and daily, changes in solar irradiance. The spectrum is created using up to six different daily proxies, and one solar flare proxy. Some of the other solar flux models currently favored by researchers are EUVAC, the Hinteregger EUV81 (HFG) model [*Hinteregger et al.*, 1981], the SOLAR2000 model [*Tobiska*, 2004], and the NRLEUV model [*Warren et al.*, 2001; *Lean et al.*, 2003]. The NRLEUV [*Warren et al.*, 2001] model is physics-based, while the other three are empirical models. *Chamberlin* [2005] demonstrated the inability of these models to accurately reproduce the solar spectrum shortward of 100 nm during solar minimum and solar maximum conditions, when compared with measurements from the SEE instrument onboard the TIMED satellite [*Chamberlin*, 2005]. There are two main reasons for this: the proxies used in the established models, and the use of older, less representative data in their creation. The other models rely on older, less numerous observations of the X-ray and VUV spectrum, although SOLAR2000 is now using the SEE data and the NRLEUV physically calculates the spectrum. This results in a less representative reference spectrum, and the models have difficulty

capturing irradiance changes due to solar cycle variations and flares. FISM is able to overcome both of these obstacles.

In order to more accurately characterize the solar irradiance, FISM makes use of more recent data from a number of satellites: the SEE instrument onboard TIMED, the two instruments on the Upper Atmosphere Research Satellite (UARS), and two on the SOlar Radiation and Climate Experiment (SORCE) satellite. Combined, these platforms yielded over 20,000 measurements spanning more than half a solar cycle, including portions of the solar cycle minimum and maximum [*Chamberlin et al.*, 2007]. Also, FISM uses six different proxies, to cover the range from 0.1–121.6 nm, and FISM can use all, some, or only one of the proxies. The $F_{10.7}$ index was found to be the least accurate proxy, but is available back to 1947 and for the foreseeable future since it is not a space-based measurement.

2.6.1   FISM Solar Flare Modeling.   Although FISM's default 60-second cadence make it ideal for use in modeling solar flare irradiance, the accuracy of the algorithm is not what it could be due to the low number, and variety of, observed flares [*Chamberlin*, 2005]. Although the SEE reference data set contained observations of over 200 flares, only 39 were used in constructing the algorithm; 26 were viewed in the impulsive phase and 13 in the gradual phase [*Chamberlin*, 2005]. The 3-second GOES $0.1 - 0.8$ nm irradiance was chosen as the best proxy for the gradual and impulsive phase. Figure 2.6a compares the FISM flare spectrum (black) with both the SEE daily average data (red), and an average of 16, 10-second measurements (blue),

which were taken during the gradual phase of a GOES X28+ flare on 4 November, 2003. The SEE level 3 (L3) data is generated by merging the daily average counts from the X-ray and EUV channels. This data has been calibrated and corrected to exclude field of view errors, data from the South Atlantic Anomaly and solar flares [*Chamberlin*, 2005]. The level 3a (L3a) data is orbit average of the same L3 data, but does include increased irradiance from flares. FISM and the level L3a data are in close agreement, and below 20 nm, are almost two orders of magnitude greater than the SEE average daily flux. This is more easily seen in Figure 2.6b. Since the figure
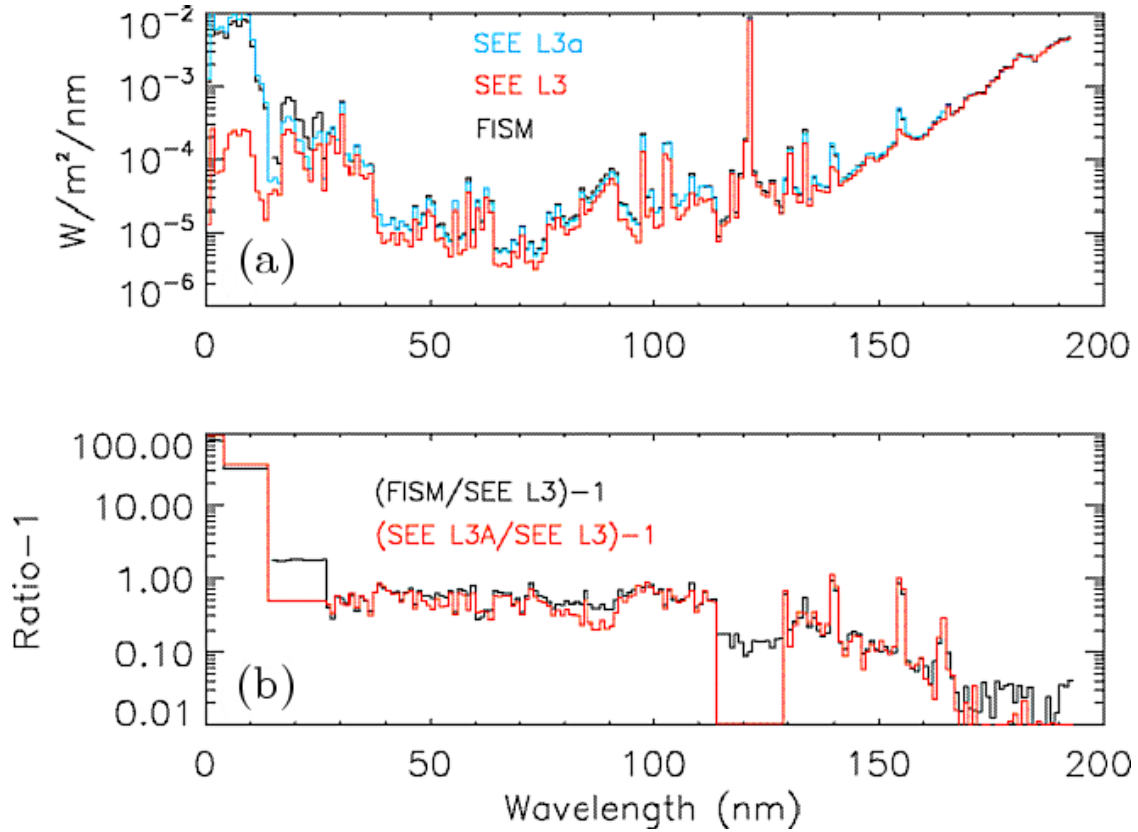
Figure 2.6.   **(a)** - Ratio of FISM and SEE for the gradual phase of an X28+ class solar flare of 11/04/03. The red line is the SEE daily average with the flare removed from the average, the black is FISM, the blue line is an average spectrum constructed from 16, 10-second observations during the flare. **(b)** - the ratio of FISM flare spectra to the SEE average daily level 3 data in red and the SEE level 3 flare spectra to the daily average in black. From *Chamberlin* [2005].

compares the ratios of FISM/L3 and L3A/L3 minus one, a 1:1 ratio is plotted as zero on the vertical axis. The L3 and L3A data appear identical between 112 and 130 nm, indicating that even during a flare this wavelength range does not increase, but no further explanation is given for this in the literature. Therefore, not only is FISM capable of producing an irradiance spectrum that varies realistically, in tandem with solar cycle variations, but it also captures the rapidly evolving spectrum when enhanced by solar flares. As the database of observed flares is sure to grow in the future, the solar flare proxy and the algorithm on which it is based will, no doubt, become more realistic.

2.7   Ionization and Photoelectrons

In the terrestrial ionosphere the three primary sources of ionization are: photoionization, secondary ionization by photoelectrons, and chemistry, often as a charge exchange reaction. Photoionization results when an energetic photon ($\lambda \leq 105$ nm) encounters a neutral gas molecule or atom, and absorption of the photon completely liberates an electron. This reaction was illustrated in Equation 2.3. In the second, the result is the same, however, the cause is an energetic (or *photo*) electron with kinetic energy exceeding the ionization threshold of the target. This is illustrated below for O^+:

$$O + e^{photo} \rightarrow O^+ + e^{photo} + e \tag{2.4}$$
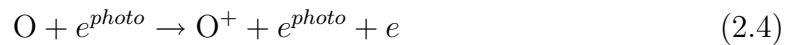
where e^{photo} is the energetic electron and e is the thermal electron liberated from O. The photoelectron still retains enough kinetic energy to ionize another neutral and

the thermal electron becomes part of the electron gas. The charge exchange reaction between N_2^+ and NO is:

$$N_2^+ + NO \rightarrow N_2 + NO^+ \qquad (2.5)$$

A fourth source is dissociative ionization (DI). DI occurs when a diatomic neutral is dissociated, and one of the resulting atoms is also ionized. This is illustrated below for N_2:

$$N_2 + h\nu \rightarrow N^+ + N + e \qquad (2.6)$$
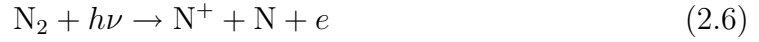
where $h\nu$ is the ionizing photon. DI increases the production rate of atomic ions, such as N^+ and O^+, while reducing the production rate of N_2^+ and O_2^+. *Richards et al.* [1994] found that photoelectrons do not have significant impact on DI, but solar flux does, causing DI rates to peak below 150 km. The relative importance of these mechanisms varies according to species, altitude, and input solar irradiance. Solar flares disproportionately enhance the XUV wavelengths, which generate more photo-electrons and cause more dissociative ionization. Of these processes, photoelectron ionization and DI are not treated in SAMI2; however, the contribution of the former is especially crucial in modeling the response of the ionosphere to solar flares.

Since ionization *is* electron production, we can think in terms of photoelectron production. From *Schunk and Nagy* [2000, Chap. 9] we see that the altitude, solar zenith angle, and energy-dependent photoelectron production rate is:

$$P_e\left(E, \chi, z\right) \; = \; \sum_l \sum_s n_s\left(z\right) \int_0^{\lambda_{si}} I_\infty \exp[-\tau\left(\lambda, \chi, z\right)] \sigma_s^i(\lambda) p_s(\lambda, E_l) d\lambda \qquad (2.7)$$

where the sum is over all energy levels l, and all individual species s. The total ion-ization cross section at each wavelength is $\sigma_s^i(\lambda)$, and the branching ratio is $p_s(\lambda, E_l)$; together they yield a cross section specific to each excited state as well as each species. The integration is carried out from 0 to λ_{si}, which is the ionization threshold for species s, and the variable E_l in the branching ratio is the energy level of the final ion state. The energy E of the photoelectron is the difference between the energy of the incoming photon, E_λ and the energy level, E_l of the ion in its excited state, minus the ionization potential (threshold) of the neutral. Therefore, the rate of photoelectron production depends on the energy of the incoming photon, and on the ionization po-tential of the neutral. The ionization potential is the minimum energy required to free an electron from the nucleus, measured in electron volts (eV). For example, H and O have ionization potentials of 13.60 and 13.62 eV, respectively, and can be ionized by a photon of $\lambda \leq 91$nm. Using H and O atoms as our example, a 91 nm photon has a little more than 13.62 eV of energy, therefore something must happen to the excess. Ignoring quantum mechanical effects, this is due to the much greater mass of the parent; there is very little recoil and almost all the excess goes into kinetic energy of the released electron. This photoelectron now continues to deposit energy into the ionosphere through two important mechanisms, secondary ionization and heating of the electron gas, although it also loses energy through excitation of the neutral gas.

Secondary ionization, as previously noted, results from ionization by an electron with kinetic energy that exceeds the ionization threshold of the target neutral. The local effect is the same as if caused by direct solar radiation, yielding an electron-ion

pair or excited state neutral; however the spatial distribution of these effects are not. The highest energy photons penetrate deeply into the atmosphere before being absorbed, far below 100 km. As a result, high energy photoelectrons are preferentially created near this region, and the high neutral density traps much of the energy here due to collisions. *Richards and Torr* [1988] found that photoelectron ionization increased the production rate of N_2^+ and O^+ by a factor of two near the production peak. In examining the Bastille Day solar flare, *Woods et al.* [2003] found that the flare caused a dramatic increase in the number of photoelectrons, particularly those generated by $2-12$ nm wavelengths.

Figure 2.7 shows the output of SAMI2, with and without photoelectron ionization. The data is for $84°$ W, $0°$ N, during solar maximum, at local noon. NO^+, O_2^+, O^+, and e are shown, and indicate large relative increases in density due to the addition of photoelectron ionization. O_2^+ increased $25-45\%$ between $100-150$ km. NO^+ increased nearly 20% at the density peak, which also decreased in altitude by 5 km. O^+ increased by roughly 40% near its peak. This is consistent with the findings of *Richards and Torr* [1988]. The changes to the NO^+ curve are indirectly caused by photoelectrons since NO^+ is generated through chemical reactions with N^+, O^+, O_2^+ and N_2^+, rather than through direct photoionization. Therefore, if the concentration of these species increases, so will the concentration of NO^+. Above 190 km, the density decrease slightly, reflecting the dependence of the NO^+ chemical production rate on the O^+ temperature, which itself is affected by the increase in the O^+ density.

28
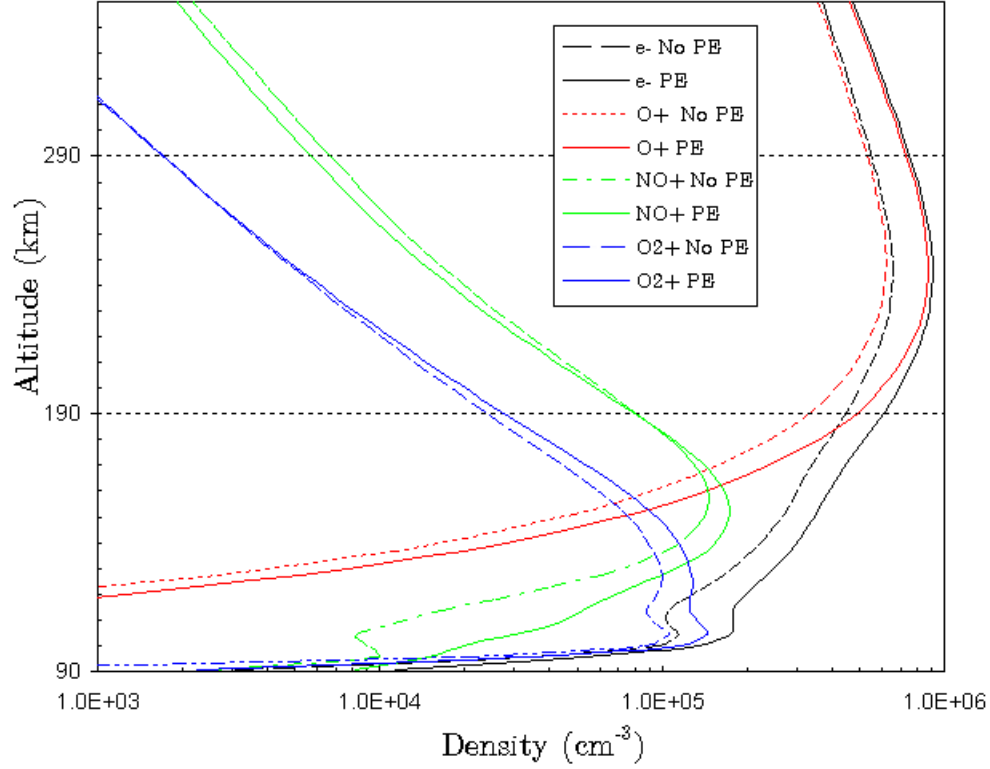
Figure 2.7.   Density of select ions and electrons, using the SAMI2 ionospheric model with (solid lines), and without (dashed lines) secondary ionization by photoelectrons. Conditions approximate high solar activity for local noon at $0°/-84°$ Lat/Lon.

The second impact of photoelectrons is in heating of the electron gas via Coulomb collisions [*Smithtro et al.*, 2005]. Also called *superthermal* electrons, to differentiate them from the cooler (less than 1 eV) background electrons, photoelectrons diffuse along magnetic field lines, cascading downward in energy at each encounter with a thermal electron, ion, or neutral. In this way they are able to deposit the original energy *non-locally*, at altitudes high above their formation and even along field lines into the conjugate hemisphere [*Woods et al.*, 2003]. This causes ion temperature to increase, ultimately increasing the individual scale heights H, and temperature-dependent chemical reaction rates. These in-turn, redefine the ion proportions, and

29

subsequently, the total electron density. The consummate result of this additional energy then, is an overall increase in ion and electron density.

This chapter introduced the reader to several topics, crucial to understanding ionospheric modeling, and the importance of solar flares. The ionosphere, a layer of plasma that surrounds the Earth, alters the propagation of electromagnetic energy that passes through it, degrading communications and GPS-based navigation. During a solar flare, the electron density increase, magnifying these effects. More detailed modeling of the ionospheric response to solar flares will allow the Air Force to understand and mitigate the impact to its systems. The SAMI2 2-D ionospheric model was selected to investigate the inter-hemispheric response to a flare; however, it requires several modifications. The temporal resolution of the input solar irradiance from EUVAC is insufficient to capture the details of the solar flare. This will be replaced by irradiance from FISM, whose 60-second cadence is sufficient to capture to fast rise and fall time of the solar flux, which drives the model ionization rate. Photoelectron, and dissociative ionization will also be added to SAMI2. Photoelectron ionization, driven by XUV energy, can increase by orders of magnitude during a flare. The next chapter focuses on the specific changes made to SAMI2.

III. Methodology

THIS chapter details the changes to SAMI2, including the modification to use the output from FISM and the tests that were run. Although SAMI2 has the temporal resolution to model the ionospheric response to a solar flare, it lacks some key components needed to do it successfully. A parameterization to account for secondary ionization from photoelectrons is added, as is the ability to utilize 60 second output from the FISM irradiance model in place of the once-per-day $F_{10.7}$ index. Finally, the SAMI2 electron gas heating scheme is replaced with a new parameterization from *Smithtro and Solomon(S&S)* [2008].

3.1   22-bin Irradiance Conversion

The move from 37-bin irradiance to 22-bins was driven by the desire to leverage the parameterization scheme of *Solomon and Qian* [2005]. This allowed the inclusion of dissociative ionization and secondary ionization by photoelectrons. The reduction in the number of bins also reduces computational time.

Solomon and Qian [2005] developed a new low-resolution irradiance scheme ($S&Q$) that provides more accurate results when compared to the 37-bin EUVAC. The EUVAC [*Richards et al.*, 1994] uses 5 nm-wide bins, and single wavelengths corresponding to solar line emission, to represent the solar irradiance from $5-105$ nm. In contrast, *Solomon and Qian* [2005] use high resolution where absorption cross sections change rapidly and coarse resolution where they change more slowly, and cover the spectrum from $0.05-105.0$ nm. The 22-bin scheme was developed by comparing a

high-resolution solar spectrum to the wavelength-dependent cross sections of O, O_2, and N_2. Through trial and error, the number of bins and boundaries were adjusted until they obtained the best agreement between the low-resolution and high-resolution (EUVAC or HFG) schemes. Since total energy deposition, as a function of altitude, is actually the sum of many Chapman functions [*Schunk and Nagy*, 2000], multiple overlapping bins are used where significant structure occurs in the solar spectrum. This allows a more accurate representation of the distribution of energy with altitude *Solomon and Qian* [2005].

The *S&Q* method includes an energy dependent ratio of secondary-to-direct ionization (p_e/p_i) to parameterize ionization by photoelectrons for each species. The ratios were calculated for each bin, and species, as function of optical depth (τ). They ran the GLOW model, for a wide variety of solar conditions, independently, for each flux bin. They concluded that p_e/p_i varied little with solar activity, and only at extremely high solar zenith angles. They also found that p_e/p_i was nearly constant with optical depth, except for $\tau \simeq 0$ [*Solomon and Qian*, 2005]. Therefore, only one value, taken at $\tau = 1$ sufficed for each bin and all altitudes. It should be emphasized that this scheme only yields the fraction of additional photoelectron ionization *locally*. Since it does not explicitly calculate fluxes of photoelectrons, non-local photoelectron effects are absent. Photoelectrons are constrained to travel along the Earth's magnetic field lines, and, in the absence of collisions, travel from one hemisphere to the other [*Woods et al.*, 2003]. *Richards and Torr* [1988] studied secondary ionization to EUV photoionization ratios and demonstrated that such transport effects were not signifi-

cant at altitudes near the ionization peak. They did find, however, that photoelectron flux could vary by up to a factor of two at high altitudes, depending on the season, due to the presence or absence of electron flux from the conjugate hemisphere.

The original EUVAC uses a reference solar flux which is based on the F74113 rocket flight (April 23, 1974) [*Richards et al.*, 1994]. The reference flux is scaled for solar activity in each wavelength bin by:

$$F_i = \text{F74113}_i \left[1 + A_i(P - 80) \right] \tag{3.1}$$

where F74113_i is the reference flux, A_i is a scaling factor and P is the proxy, given by:

$$P = (\langle F_{10.7} \rangle + F_{10.7})/2 \tag{3.2}$$

Values appropriate to the 22-bin scheme for A_i and the reference flux are given by *Solomon and Qian* [2005], as are cross sections for O, N_2, and O_2. Cross sections for He and N were calculated by *Smithtro* [private communication].

Figure 3.1 compares SAMI2, using the old 37-bin EUVAC and the new *S&Q* 22-bin EUVAC, without photoelectrons. The figure shows the photoion production rate (cm^{-3} s^{-1}) near local noon at 0.0° N, 84.0° W, which has a magnetic latitude of 11° N. Solid lines represent the 37-bin model and dashed lines represent the new low-resolution bin structure. The major differences are significant increases in the production rates of O^+ and O_2^+ below 180 km and 125 km, respectively. Near 120 km, O^+ production roughly doubles, and near 100 km the increase is by more than 300%,

but it is only greater by $10-40\%$ in the vicinity of the peak. On the other hand, O_2^+ production increases by an order of magnitude between 100 and 125 km, shifting the altitude of peak production downward by about 20 km. A mid-latitude comparison (not shown) at $40.0°$ N, $84.0°$ W showed similar results. This shows that the new scheme works equally well in the low and mid-latitudes.
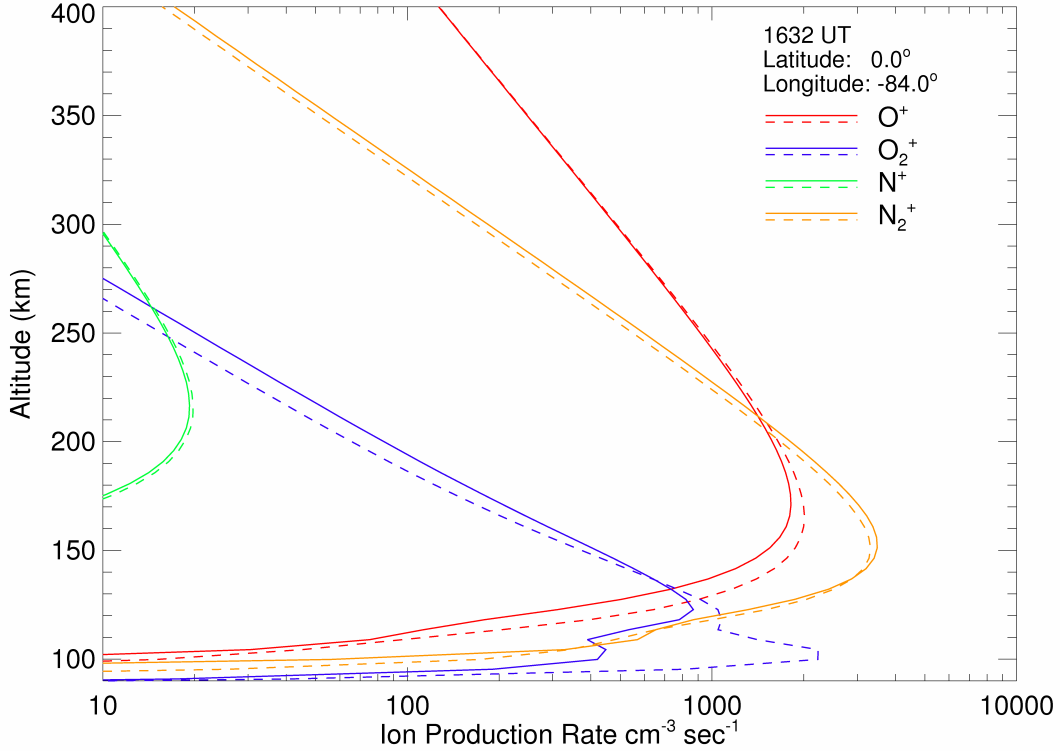
Figure 3.1.   Ion production rate (cm^{-3} s^{-1}) from photoionization using the 37-bin EUVAC (solid lines) and 22-bin $S\&Q$ (dashed lines) irradiance schemes in SAMI2, for four major species (He^+ not shown). Solar conditions approximate solar maximum ($F_{10.7}=187$), near local noon for $0.0°$ N/$84.0°$ W.

The increase in O^+ production is primarily due to the increased ionization by wavelengths shortward of 5 nm, which are not included in EUVAC. For O_2^+, the main cause is increased ionization by wavelengths greater than 91.4 nm, where the O_2 cross sections are larger than those in the EUVAC and the other species have cross sections

of zero. This figure does not reflect the importance of dissociative ionization, which for $\lambda \leq 3$ nm, would increase the production of O^+ rather than O_2^+.

It should be emphasized that the original version of SAMI2, using the 37-bin EUVAC, uses ionization cross sections for O_2 and N_2 which are, in fact, the full absorption cross sections. In reality, a fraction of the total absorption cross sections result in dissociative ionization, yielding O^+ and N^+. This causes the original version to over-estimate production of O_2^+ and N_2^+, and underestimate O^+ and N^+. For example, the ionization cross section for O_2^+ from 10 - 15 nm is 3.81×10^{-18} cm^2 in the original SAMI2; however, the correct cross section should be 2.35×10^{-18} cm^2, with the difference, 1.46×10^{-18} cm^2, being the cross section for dissociative ionization of O_2 resulting in O^+ [*Schunk and Nagy*, 2000]. It was deemed more prudent to begin the 22-bin conversion, using the correct ionization cross sections and ignoring, for the present, dissociative ionization. Even using cross-sections that should over-estimate the production of O_2^+ and N_2^+ while under-estimating O^+ and N^+, the 37-bin version still under-estimates O_2^+ production below 110 km when compared to the 22-bin version.

Figure 3.2 shows the resulting ion densities (cm^{-3}) for the same model runs. As in Figure 3.1, the 37-bin and 22-bin schemes are represented by solid and dashed lines, respectively. Consistent with the minimal change observed in the production rate of N^+, the N^+ density shows only slight changes, while the decrease in production rate of N_2^+ is clearly reflected in the decrease in density. The electron density is driven by the changes in O^+ above 155 km and O_2^+ below, the latter, increasing by a factor of

1.7 and generating a clearly defined E region peak at 107 km. Near and above the F$_2$ region peak at 350 km there is virtually no difference between the schemes, so this region of the plot is not shown.
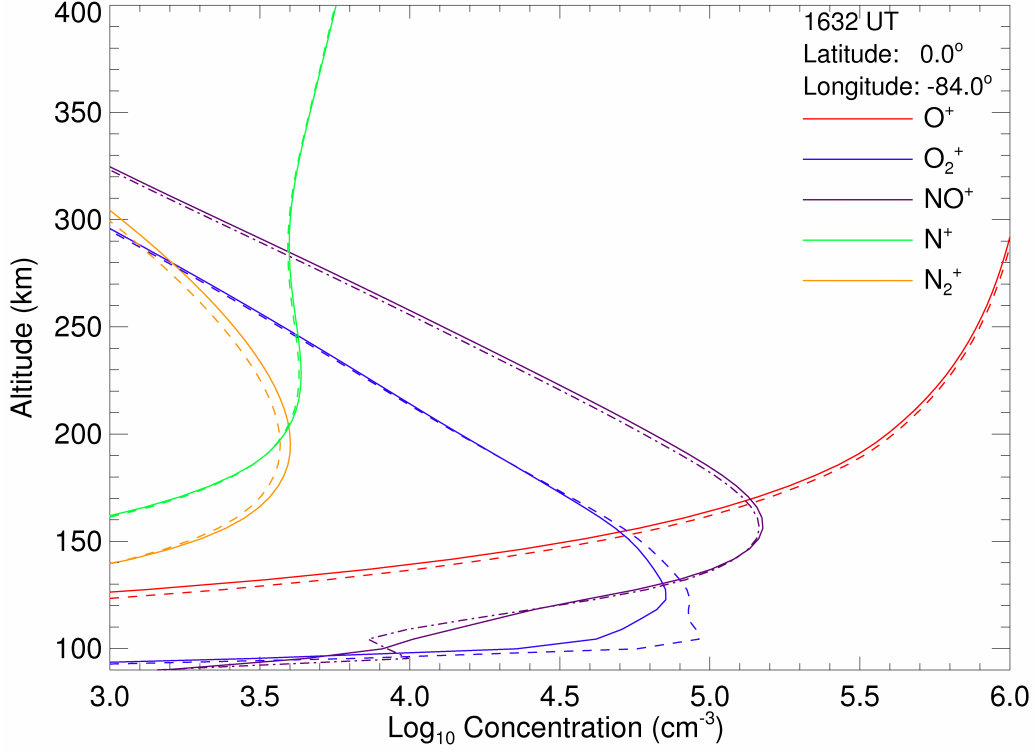

Figure 3.2.   Ion density (cm^{-3}) from SAMI2 using the 37-bin EUVAC (solid lines) and 22-bin $S\mathcal{E}Q$ (dashed lines) irradiance schemes.   Five major ion species are shown. Solar conditions approximate solar maximum ($F_{10.7} = 187$), near local noon for 0.0° N/84.0° W.

3.2 Addition of Dissociative and Photoelectron Ionization

Two vital components of the $S\&Q$ scheme are the parameterizations that account for secondary ionization by photoelectrons and dissociative ionization (DI). Enabling SAMI2 to take advantage of these required reworking the portion of the model code that calculates the photoionization rate for each species. In the original version, the photoionization rate q, of species l, at altitude z, is calculated by:

$$q_l(z) = \underbrace{n_l(z) \sum_{\lambda} \sigma_l^i(\lambda) \, \mathrm{F}_i(\lambda)}_{a} \underbrace{\exp\left[-\sum_{m} \sigma_m^a(\lambda) \int_z^{\infty} n_m(s) ds\right]}_{b} \qquad (3.3)$$

where, $n_l(z)$ is the density of the neutral species l at z, and σ_l^i is the ionization cross section of the lth neutral [*Huba et al.*, 2000]. Part b yields the ionizing flux at height z, based on the incident solar flux, $\mathrm{F}_i(\lambda)$, and the absorption of the flux based on the absorption cross section σ_m^a of species m. Only O, O_2, and N_2 are treated as significant absorbers of the incoming flux.

In the new calculation, part b is essentially unchanged, however, the calculation is now held in an array of the flux for each wavelength bin at height z shown below:

$$q_l(z) = \sum_{\lambda} n_l(z)\sigma_l^i(\lambda)\phi_z(\lambda) \qquad (3.4)$$

where $\phi_z(\lambda)$ irradiance at height z. Moving $n_l(z)$ inside the summation allows straightforward calculation of photoelectron ionization and DI by applying of the appropriate ratios from *Solomon and Qian* [2005] to the calculated photoionization rate. This

yields:

$$q_l^{total}(z) = q_l^{p_i}(z) + q_l^{p_e}(z) + q_l^{p_{DI}}(z) \tag{3.5}$$

where $q_l^{p_i}$ is direct photoionization, $q_l^{p_e}$ is ionization rate due to photoelectrons, and $q_l^{p_{DI}}(z)$ is the rate due to DI. Multiplying Equation 3.4 by the secondary ionization ratio p_e/p_i, yields the ionization rate due to secondary ionization, while DI is calculated by using the appropriate cross section for σ_l^i. Below is an example of calculating the secondary ionization rate:

$$q_l^{p_e}(z) = \sum_\lambda p_e/p_i(\lambda)n_l(z)\sigma_l^i(\lambda)\phi_z(\lambda). \tag{3.6}$$

Before adding photoelectron ionization, it is appropriate to first discuss the impact of properly treating DI. Figure 3.3 shows the ion production rate $(\text{cm}^{-3}\ \text{s}^{-1})$ for the *S&Q* scheme. The solid lines indicate the production rate using the absorption cross sections (as in the original 37-bin SAMI2) for O_2 and N_2, instead of the smaller O_2^+ and N_2^+ ionization cross sections given by *Solomon and Qian* [2005]. O^+ and N^+ are calculated using the same ionization cross sections as in Section 3.1, however there are no additional ions produced from the dissociative ionization of O_2 and N_2, respectively. The dashed lines indicate the model run with the DI fractions from O_2 and N_2 added to the production of O^+ and N^+. At this point the corresponding fractions are now absent from O_2^+ and N_2^+.

As expected, properly accounting for dissociative ionization reduces the production rates of O_2^+ and N_2^+ and increases the rates of O^+ and N^+. Neglecting DI

38

overestimates the production of O_2^+ and N_2^+ by factors of 7 and 2, respectively. Both O^+ and N^+ show increases at the same altitude as the greatest decreases for O_2^+ and N_2^+. In the case of O^+, this results in a relatively large increase far below the production peak and only a slight change at the peak. On the other hand, the increase for N^+ is by more than three orders of magnitude, lowering the altitude of peak production to 139 km. Near the altitude of the N^+ density peak (See Figure 3.4) at 300 km, the increase is a more modest factor of 2.9.
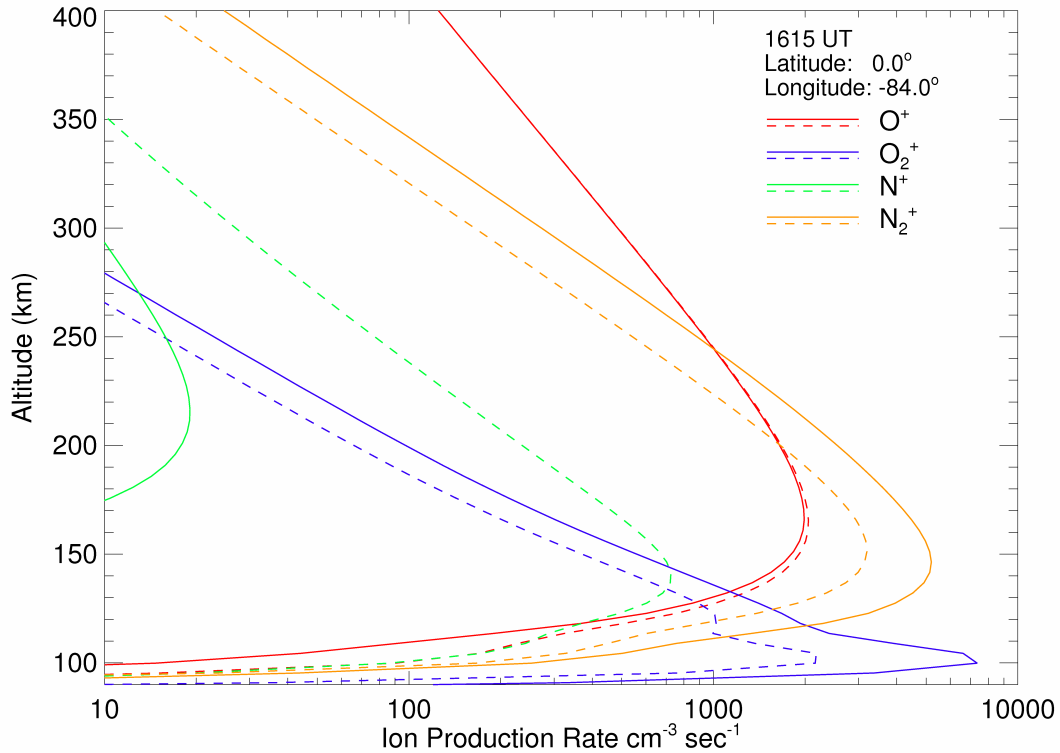
Figure 3.3.   Ion production rate (cm^{-3} s^{-1}) for SAMI2 using the 22-bin $S\mathcal{E}Q$ irradiance scheme with (dashed lines) and without (solid lines) dissociative ionization for four major species. Photoelectron ionization is not included. Solar conditions approximate solar maximum ($F_{10.7}=187$), near local noon for 0.0° N/84.0° W.

Figure 3.4 shows the resulting ion and electron densities (cm^{-3}) for the $S\mathcal{E}Q$ scheme with (dashed), and without (solid) the correction for dissociative ionization.

The effect on the electron density is minimal above 200 km. The decrease in total electron density from ~ 125 to 200 km, despite an increase in the density of O_2^+, is a result of the off-setting *decrease* in the density of NO^+ (not shown), which is generated solely through chemical reactions. In this range, the NO^+ concentration is an order of magnitude greater than that of O_2^+, the decrease of the former overwhelming the increase from the latter. By 185 km, the O^+ density is an order of magnitude greater than NO^+ and completely dominates the plasma by 200 km.

Figure 3.4.   Ion density (cm^{-3}) for 22-bin *S&Q* without (solid lines) and with (dashed lines) proper accounting for di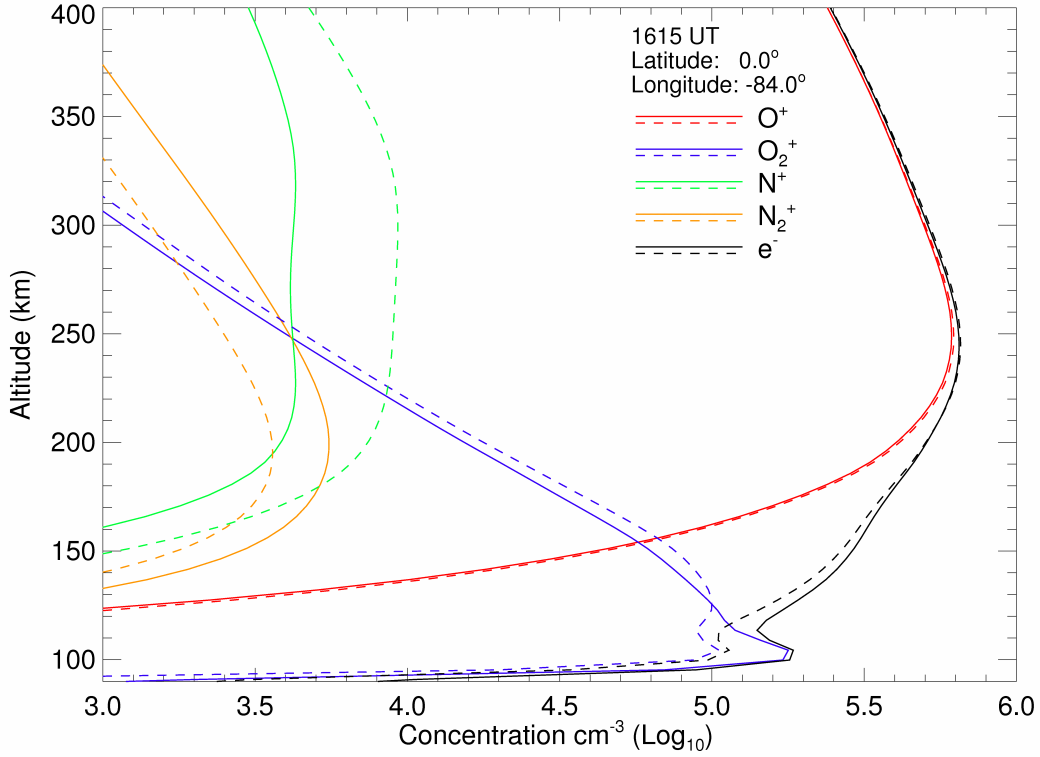ssociative ionization. Solar conditions approximate solar maximum ($F_{10.7} = 187$), near local noon for 0.0° N/84.0° W.

Figure 3.5 shows the result of including the parameterization for photoelectron impact ionization on the ion production rate (cm^{-3} s^{-1}). The most dramatic effects

are seen between 100 and 150 km, especially in the greater production of N_2^+, which

increases by an order of magnitude from $100 - 120$ km and by $\sim 60 - 100\%$ in the

vicinity of the production peak at 140 km. Similarly, O^+ increases by an order of

magnitude at 100 km, decreasing to a 100% increase at 100 km and to a 40% increase

at 240 km, which remains roughly constant up to 400 km. The change in O_2^+ is less

pronounced, reaching a peak increase of 40% at 110 km. N^+ experiences an order

of magnitude increase from 100 to 148 km, resulting in a double-peak profile, with a

secondary maximum at 110 km. Likewise, the production peak of N_2^+ drops from 150

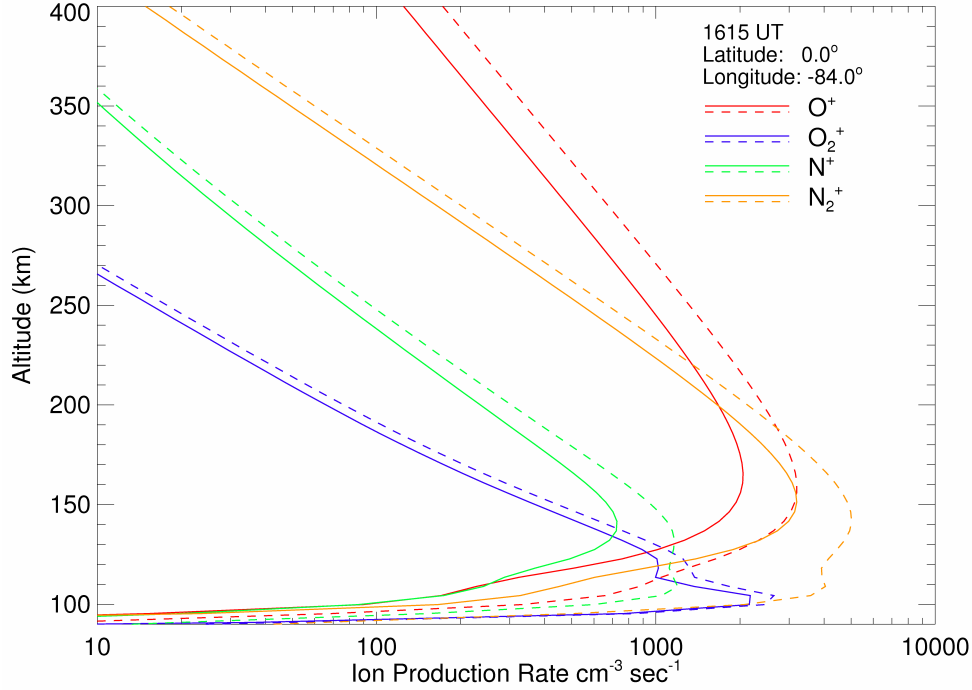to 140 km, however it also developes a well-defined valley and secondary peak below

120 km.

Figure 3.5. Plot of ion production rate $(\text{cm}^{-3} \text{ s}^{-1})$ for 22-bin *S&Q* with (dashed lines) and without (solid lines) inclusion of secondary ionization from photoelectrons. Dissociative ionization is also included. Solar conditions approximate solar maximum $(F_{10.7} = 187)$, near local noon for 0.0° N/84.0° W.

Figure 3.6 shows the resulting changes to the ion and electron density (cm^{-3}) for the same model runs. The overall electron density increases by roughly 70% near 110 km. The difference decreases above this point, dropping to a 30% increase by 165 km, before increasing to 40% at the F_2 peak. In order to gauge the effect of the
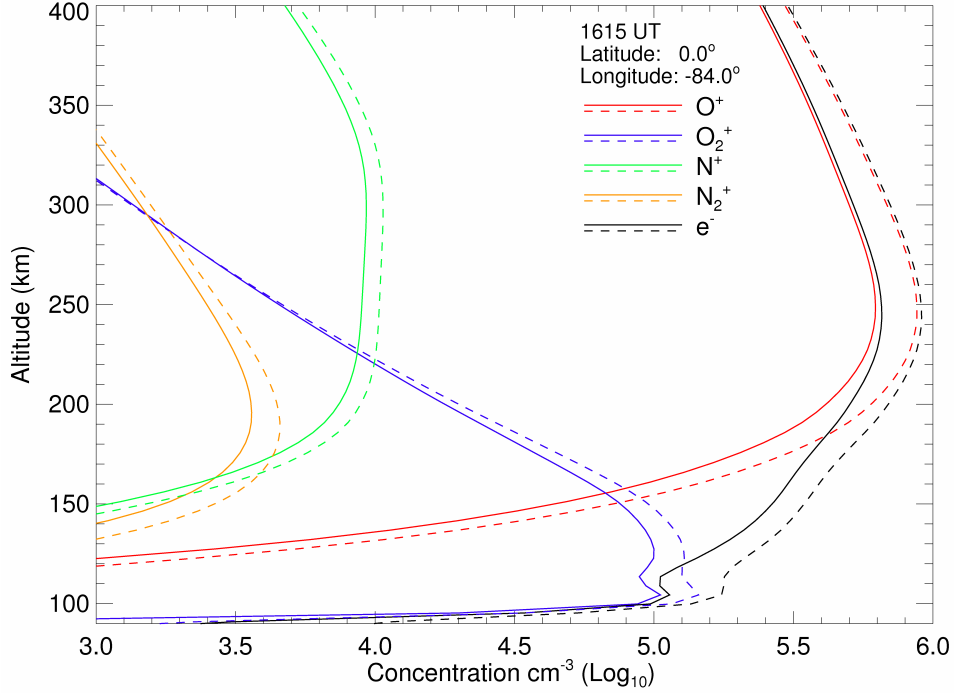
Figure 3.6.   Ion density (cm^{-3}) for SAMI2 using the 22-bin $S\&Q$ with (dashed lines) and without (solid lines) inclusion of secondary ionization from photoelectrons. Dissociative ionization is also included. Solar conditions approximate solar maximum $(F_{10.7}=187)$ near local noon for $0.0°$ N/$84.0°$ W.

$S\&Q$ scheme in SAMI2, the 37-bin and final 22-bin models were both compared to a figure from *Solomon and Qian* [2005]. Although a quantitative assessment was not possible, Figure 6a of *Solomon and Qian* [2005] offers a qualitative comparison to another model. Figure 3.7a shows the O_2^+, O^+, NO^+, and electron densities for the 37-bin (solid lines) and 22-bin versions of SAMI2. The latter includes dissociative and photoelectron ionization. Figure 3.7b is taken from *Solomon and Qian* [2005] where

they used the NCAR Thermosphere Ionosphere Electrodynamics General Circulation (TIE-GCM) model to test the efficacy of the low resolution scheme. They conducted three model runs using: the standard 37-bin EUVAC flux, the 22-bin low-resolution scheme for the EUVAC, and 22-bins with measurements taken from the SEE instrument in place of the EUVAC baseline flux. The model was run for 27.5° N, 165.0° W at noon during solar maximum ($F_{10.7} = 188$, and $\langle F_{10.7} \rangle = 186$). The most striking change between the 37 and 22-bin versions of SAMI2 is the development of an E region between 100 and 120 km. In this region

| | (a) | | (b) |
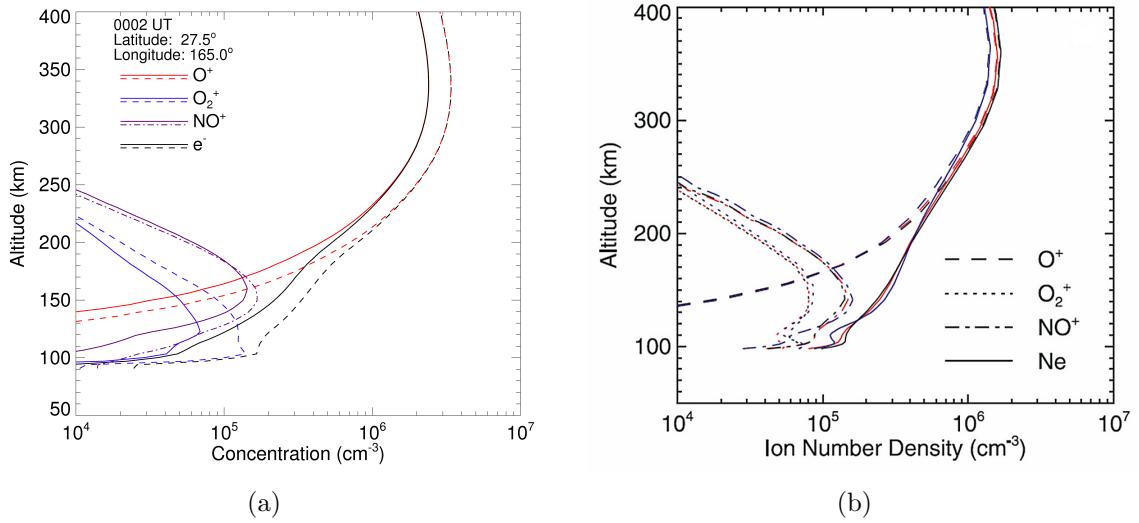
Figure 3.7.   (a) Ion density (cm^{-3}) for SAMI2, using 37-bin EUVAC (solid lines), and 22-bin *S & Q* scheme (dashed lines). (b) Ion density resulting from several irradiance schemes applied to the NCAR TIE-GCM model. Blue: 37-bin EUVAC; red: EUVAC modified for 22-bins; black: 22-bin scheme using TIMED/SEE irradiance. Solar conditions are the same for SAMI2 and TIE-GSM; $F_{10.7} = 188$, and $\langle F_{10.7} \rangle = 186$ for local noon (0 UT) at 27.5° N/165.0° E. Adapted from *Solomon and Qian* [2005].

the electron density increased by more than an order of magnitude, driven by a comparable increase in the O_2^+ density. At the F_2 peak, the new scheme yields an electron density that is about 130% larger than the TIE-GCM, and roughly 50% larger than the original version of SAMI2. Having made the transition to 22-bins, adding DI and photoelectron ionization, the next step improves the way SAMI2 handles photoelectron heating.

3.3 Electron Volume Heating Rate

As discussed previously, the importance of photoelectrons is difficult to ignore at low altitudes where they are responsible for a significant portion of the total ionization rate. A second, equally important effect is the heating of the thermal (ambient) electron gas, which in turn heats the ion gas through Coulomb collisions. Specification of the electron (T_e) and ion temperature is crucial to calculating species scale heights (H), and chemical reaction rates. The electron temperature depends on the volume heating rate (eV cm^{-3} s^{-1}), however, due to its dependence on the photoelectron flux, which is often parameterized, it is usually not calculated explicitly [*Smithtro and Solomon*, 2008]. From *Schunk and Nagy* [2000], the electron temperature is calculated by:

$$\frac{\partial T_e}{\partial t} - \frac{2}{3}\frac{1}{n_e k_b}\underbrace{b_s^2\frac{\partial}{\partial s}K_e\frac{\partial T_e}{\partial s}}_{a} = -Q_{en} - Q_{ei} + Q_{phe} \tag{3.7}$$

where a is the heat flux along the magnetic field line (s) in the dipole coordinate system. The cooling terms Q_{en} and Q_{ei} are due to electron-neutral and electron-ion collisions, respectively, and Q_{phe} is the heating due to photoelectrons [*Huba et al.*, 2000]. Following the work of *Millward et al.* [1996], the ionosphere is divided into two regimes. The first is a low-altitude regime in which collisions cause local photoelectron heating. The second, a high-altitude regime, is dominated by transport and heating is non-local. In the local regime, a parameterization from *Swartz and Nisbet* [1972] (SN) is used to calculate the volume heating rate:

$$Q_{phe} = \varepsilon P_{phion} \tag{3.8}$$

where the volume heating rate from photoelectrons, Q_{phe}, is determined by the photoionization rate P_{phion}, and average heating efficiency, ε. The heating efficiency is given by:

$$\varepsilon = \exp[-f(R)] \tag{3.9}$$

where $f(R)$ is a fourth-order polynomial fit to a deposition efficiency R given by:

$$f(R) = 12.75 + 6.941R + 1.66R^2 + 0.08034R^3 + 0.001996R^4 \tag{3.10}$$

$$R = \ln\left[\frac{n_e}{n_{O_2} + n_{N_2} + 0.1n_O}\right] \tag{3.11}$$

In the non-local, high-altitude regime, photoelectron production is nil, therefore, the volume heating rate is calculated as an exponential decreasing function of the integrated electron density along the field line:

$$Q(s)_{phe} = \frac{b(s)}{b_0} n_e q_0 \exp\left[-C \int_{s_0}^{s} n_e ds\right] \qquad (3.12)$$

where q_0 is the heating rate per electron (eV/s), $q_0 = Q/n_e$, calculated at the altitude, s_0, of the transition from local to non-local heating. The ratio $\frac{b(s)}{b_0}$ accounts for expansion of the flux tube with b_0 as the field strength at the transition point. The integral is calculated from $s_0 \rightarrow s$, or from the transition point to the current position, s. The transition points are determined where $R \simeq 10^{-3}$, which limits the transition altitude to approximately to about 325 km.

The *SN* 4th-order fit was replaced with a new 6th-order fit from *Smithtro and Solomon* [2008] (*SS*), and a new deposition efficiency:

$$R^* = \ln\left[\frac{n_e}{n_{O_2} + n_{N_2} + n_O}\right] \qquad (3.13)$$

where the total density of O, n_O, is used instead of 10% of the total density. *Smithtro and Solomon* [2008] demonstrate that the *SN* fit no longer provides the best possible approximation to a *full-physics* treatment, especially in light of advances in the measurement of the solar XUV flux and key cross sections, since it was proposed 35

years ago. Also, unlike the *SN* model, the *SS* scheme is capable of reproducing the heating due to large solar flares.

The *SS* method treats the local-regime, Q_{phe}, using three broad wavelength bands, $0-55$ nm, $55-80$ nm, and $80-105$ nm. The heating contribution from the 2nd and 3rd bands are calculated by equation 3.8, while the $0-55$ nm band is found by tabulating a running sum of the ionization rate times the average photon energy in each wavelength bin, then multiplying the sum by a normalized heating efficiency per ionization:

$$Q_{phe}^{0-55} = \varepsilon \sum_i P_i \bar{\varepsilon}_i \tag{3.14}$$

where i denotes the individual wavelength bins [*Smithtro and Solomon*, 2008]. The normalized heating efficiency, ϵ, is calculated using equation 3.9 with the new sixth-order fit and R^* from *Smithtro and Solomon* [2008]. As long as the field lines remain wholly within one regime, only possible for near-equatorial lines, the volume heating rate is a smooth curve, invoking only equation 3.8. Since most field lines *do* cross the transition point, both equation 3.8 and equation 3.12 must be reconciled across this boundary.

The transition between the local and non-local regime presents a challenge due to the formation of a discontinuity as shown in Figure 3.8. It was found that the discontinuity formed at the transition point when using the conjugate transition point as the upper limit in the integral from equation 3.12. In the original SAMI2, the discontinuity is smoothed, however, at low solar activity levels, the discontinuity is still

present. The alternative is to extend the upper limit of equation 3.12 to the footpoint of the field line. Although this incorrectly extends the non-local approximation into the collisional regime, the relative increase above the local heating is generally less than 10% for high $F_{10.7}$ values. Figure 3.8 shows the electron volume heating rate (eV/cm^{3}s) versus altitude along a field line for both low and high solar activity. The southern hemisphere portion of the field line is on the left, the northern portion on the right. At low solar activity Figure 3.8a, the discontinuity at the transition point is visible using both the SN and SS parameterizations. The lower transition height using the SN causes q_0 in equation 3.12 to start out much greater than in the SS version, causing the resulting volume heating rate to remain higher at all altitudes. The greatest difference between the SS volume heating method occurs just below the transition point due to the contribution from the non-local conjugate hemisphere. Since the non-local volume heating rate goes as an inverse exponential of the electron density, the contribution rapidly decreases as the altitude approaches the electron density peak, at around 230 km. At low solar activity, the relative difference at the southern transition height of 311 km is 43%, but rapidly decreases to less than 10% by 220 km, a pattern that is mirrored in the northern hemisphere. Above the transition points, the maximum relative difference is around 4%, from $1100-1600$ km in both hemispheres, but is generally $\leq 2\%$ up to the maximum altitude of 10,000 km. At very low altitudes the new scheme results in heating rates that are tens of percent, to an order of magnitude, greater than SN, especially below 120 km.

In Figure 3.8b, at high solar activity, a similar pattern exists, however there are some important differences. The new algorithm is valid to a much greater altitude than the SN fit and the improved 6th order fit generates higher heating rates in the local region. Although it is not discernible in Figure 3.8b, the transition altitude is 279 km, which is the same as in Figure 3.8a; however, atmospheric expansion under the increased solar activity should raise the transition height. This change is seen using the SS method. Using the new 6th order fit and R value, the SS method supports a much higher transition height of 490 and 470 km, in the northern and southern hemispheres, respectively. As a result, the SN volume heating rate transitions to the non-local equation too soon, resulting in a heating rates that are too low above the transition point. The increased heating rates below the peak directly result from the incorporation of increased short wavelength irradiance into the design of the new fit. This results in up to a factor of four increase in the volume heating rate near 100 km and a 90% increase at 110 km. The two methods were compared for a variety of field line locations, times of year, and levels of solar activity. The same general results held for all conditions so are not shown. It was noted, however, that when the solar zenith angle, χ, was greater than around 80°, i.e., one footpoint was in shadow while the other was near local noon, the differcences between the methods was greatly reduced.
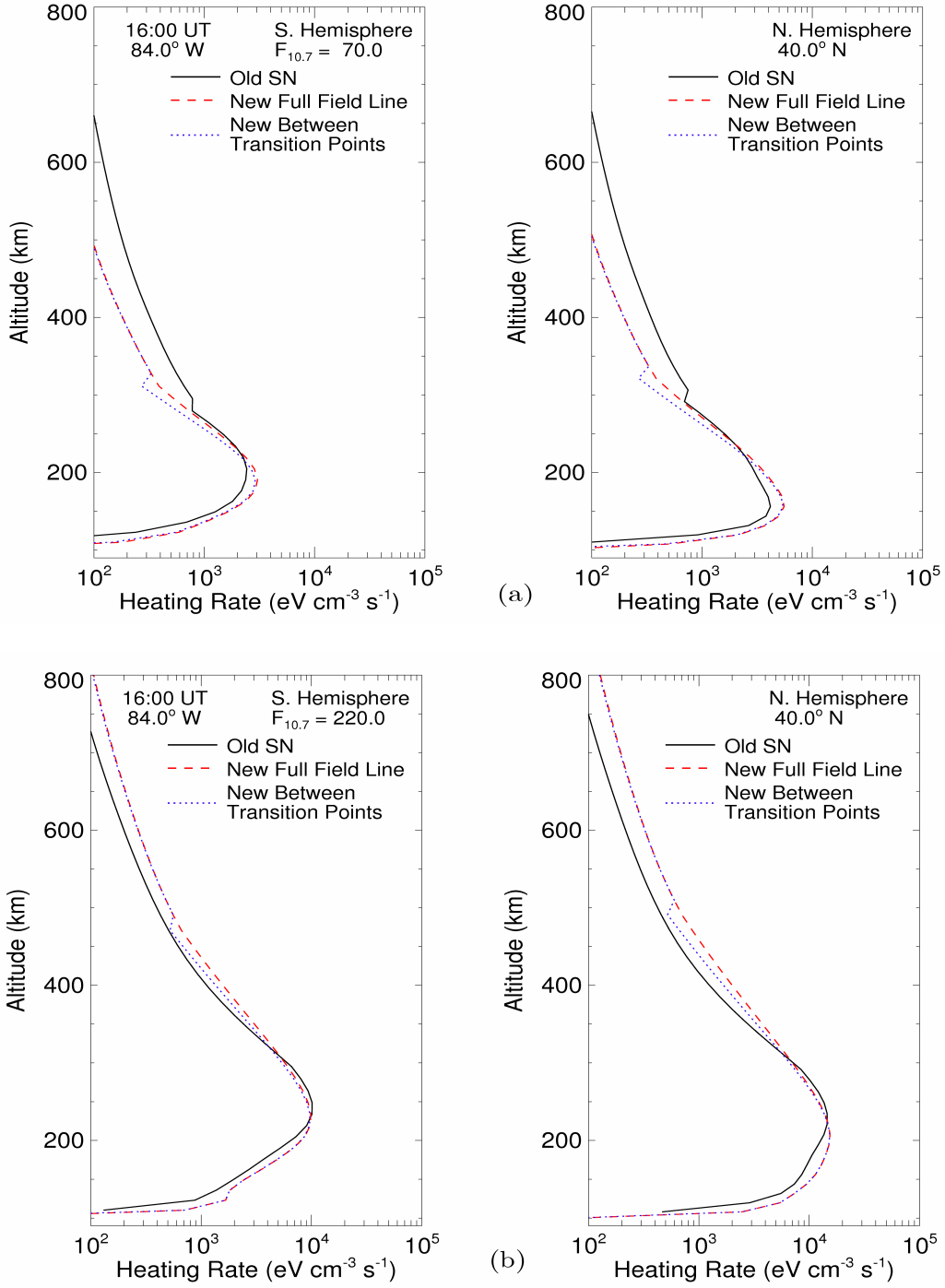
Figure 3.8. Electron volume heating rate along a field line using the parameterization of *Swartz and Nisbet* [1972] (solid), and *Smithtro and Solomon* [2008] using the conjugate transition point as the upper limit for the non-local regime integral (dotted) and the conjugate footpoint as the upper limit (dashed). The time is near local noon on the vernal equinox to ensure the same solar zenith angle in both hemispheres. **(a)** Conditions approximate solar minimum. **(b)** Conditions approximate solar maximum.

3.4 Adding Irradiance from FISM

To complete the modifications two final changes were made to the code. The first involved bracketing the time of interest with a higher data output frequency. This allowed the model to run as before, with data output at 15-minute intervals, except during the time of the flare, when the output frequency increases to 1-minute intervals.

The second change modified SAMI2 to read the 60 second irradiance data from the FISM model, which was described in Section 2.6. FISM provides the irradiance values in 1 nm-wide bins from $0.5 - 192.5$ nm, however, the Solomon and Qian 22-bin photoionization scheme includes irradiance bins of $0.05 - 0.4$ nm and $0.4 - 0.8$ nm. The FISM files, covering period from $00 - 23{:}59$ UT, were combined with the GOES-12 1-minute $0.04 - 0.5$ nm and $0.1 - 0.8$ nm X-ray flux ($NGDC$), using a data parsing utility from *Smithtro* [private communication].

In order to minimize any spikes caused by mixing EUVAC and FISM, the FISM irradiance at 00 UT was used in place of the EUVAC irradiance until the *begin-flare* time, specified in the SAMI2 input file, was reached. The model would then update the irradiance every 60 seconds, using FISM, from that point until the end of the run. Some computational time may be lost by the additional calls to read the FISM file after the end of the flare; however, elevated irradiance may persist for an hour or more beyond the flare peak, which would impact the post-flare evolution of the ionosphere.

This summarizes the major changes to SAMI2, making it suitable for analyzing the effects of solar flares. Many smaller changes were made in the course of debugging and ensuring the correct implementation of the aforementioned alterations to the model physics, however, these are not worth discussing further. This chapter summarized the modifications made to SAMI2 in order to use it to model solar flare. First, the 37-bin EUVAC irradiance model was modified according to *Solomon and Qian* [2005]. This also incorporated parameterizations for dissociative and photoelectron ionization. Next, the original photoelectron heating scheme was modified in favor of a new method from *Smithtro and Solomon* [2008]. Finally, SAMI2 was modified to enable the use of high-cadence, high-resolution irradiance from FISM [*Chamberlin et al.*, 2007]. SAMI2 can now be used to model the ionospheric response to a flare.

IV.   Results

THIS chapter describes the results from using the modified version of SAMI2 to model the ionospheric response to the X17 flare of 28 October, 2003. A brief discussion of the flare itself will be followed by analyzing the differences over a broad hemispheric view, then narrowing the discussion to focus on two specific altitude and latitude areas. The results will focus on the changes in ionospheric temperatures and their relationship to changes in electron density, and what can be inferred about the processes that drive these changes.

4.1   X17 Solar Flare, 28 October, 2003

On 28 October, 2003 an X17.2 solar flare erupted from solar active region 10486, peaking at 1110 UT, as measured by the GOES X-ray detector. It was nearly centered on the solar disk and is currently the fourth largest flare on record and was chosen, first and foremost, because it is a large, well-studied flare. The extreme increase at X-ray and XUV, provide a *worst-case* scenario to the model, thus putting the modifications through their paces. Also, having been the subject of many studies, it was thought that some of the previous work might provide useful benchmarks for the results of this simulation. Figure 4.1 shows the ratio of flare to pre-flare photon flux for the high resolution FISM (solid red), and the 22-bin (solid black). The ratio is the flux at the flare peak divided by the flux at 0900 UT. Since FISM is the primary driver to the 22-bin flux, they should be very similar. This assumption is correct, except at the shortest wavelengths $(0-1$ nm$)$, where FISM extends coarsely. The inset shows the

corresponding GOES-12 solar irradiance from the 0.1−0.8 nm channel with the times chosen for the ratio depicted by the vertical dashed lines. 0900 UT was chosen as being representative of the pre-flare irradiance. The shortest wavelengths increase during the flare by more than an order of magnitude, and in the case of the 0.05−0.4 nm bin, by 4 orders of magnitude, which is beyond the upper limit of the plot.
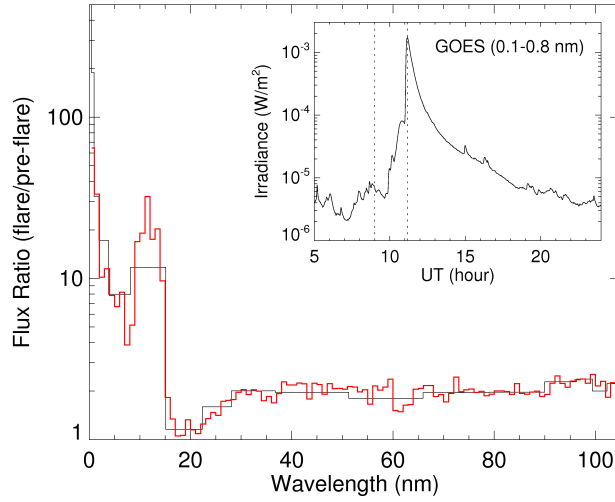
Figure 4.1.   Ratio of flare to pre-flare photon flux (photons cm^{-2}s^{-1}) for the X17 flare of 28 October, 2003. **(Inset)** Solar irradiance in (W m^{-2}) from the GOES-12 0.1−0.8 nm X-ray channel. Vertical dashed lines indicate the times (UT) used in computing the ratio.

The version of SAMI2 used in this simulation included the changes described in previous chapter: secondary ionization by photoelectrons, dissociative ionization, *Smithtro and Solomon* photoelectron heating scheme, and the *Solomon and Qian* (*S&Q*) irradiance scheme. The FISM output, from [*Chamberlin et al.*, 2007], and GOES-12 0.1−0.8 nm and 0.05−0.4 nm flux data for 28 October, 2003 are combined into the the 22-bin *S&Q* format via the parsing program mentioned in Section 3.4. The model is run twice, the difference between the runs being that the *flare* run includes

the 60-second FISM irradiance, while the *non-flare* run uses only the FISM irradiance from 00 UT . Alternately, the model can be run using the EUVAC irradiance, however, this can cause unnecessary transients in the output.

The model grid, being a hemispheric slice, is defined by the equatorial (0° magnetic) height of the lowest and highest magnetic field lines. The sub-solar point at 11 UT is ∼ 15.0° E, and the minimum and maximum field line heights over the magnetic equator (8.0° N geographic) were 90 and 7000 km, respectively. This equates to the endpoints of the highest altitude field line at 38.0° S and 52.0° N, although the output domain is somewhat less due to the curvature of the field lines. The dip angle of the field lines in the mid-latitudes dictates a high number of field lines in order to obtain adequate low-altitude resolution, however, the model run time is largely dictated by the resolution of the grid. In order to keep run times down, the number of field lines are kept to 228 or less, and the number of grid points per field line, to 201. Increasing the number of grid points beyond this made did not improve the output, but did increase the run time by several hours. The input parameters are shown in Appendix A.

4.2 Hemispheric Differences

4.2.1 Height and Peak Density at the F2 peak, and TEC. The ionosphere exhibits differences between the hemispheres on diurnal, seasonal, and solar cycle scales. Despite being two months away from the winter solstice, the pre-flare ion density clearly shows the winter anomaly, characterized by asymmetrical maxima in

the electron density (n_e), shown in Figure 4.2a. This figure shows the electron density in cm^{-3} using the FISM 60-second flare irradiance, but 10 minutes before the flare peak (1110 UT/1210 L). The solid line indicates the height (km) of the F$_2$ peak (H_mF_2), calculated with a FORTRAN function supplied by the model author [*Huba*, 2007]. When compared to the no-flare plot (not shown), the flare run shows small increases in both n_e and latitudinal extent of the peaks, but is otherwise representative of the no-flare condition of the ionosphere. As predicted by the seasonal anomaly, in the winter (northern) hemisphere, the H_mF_2 is lower and the density at the F$_2$ peak is higher. Also, while the S. Hemisphere maximum covers a broad extent, both in terms of height and latitude, the N. Hemisphere maximum is much more limited. Worth noting is the deep trough in n_e at 37° N; the Log$_{10}$ = 6.0 contour more than 300 km lower than in the S. Hemisphere. Figure 4.2 b shows the electron density 29 minutes after the flare peak; the two maxima have increased substantially in magnitude and, south of 20° N, H_mF_2 has lowered at nearly all latitudes. The odd time of the output is a function of the resumption of low-cadence output at 1139 UT. This lowering of the H_mF_2 is particularly noticeable near 3.0° S as the H_mF_2 has lowered from 550 km to $\sim$350 km. This, however, seems to be a function of the steepness of the contours, rather than a significant change in the overall shape.

Figure 4.3 illustrates the difference between the flare and non-flare model runs at 1139 UT in the model domain from 36° S to 48° N. Total electron content (TEC) $(1 \times 10^{16}$ m$^{-2})$ and electron density (cm^{-3}) at the F$_2$ peak (N_mF_2) are shown in Figure 4.3a, while Figure 4.3b shows H_mF_2. Dashed lines indicate the run without
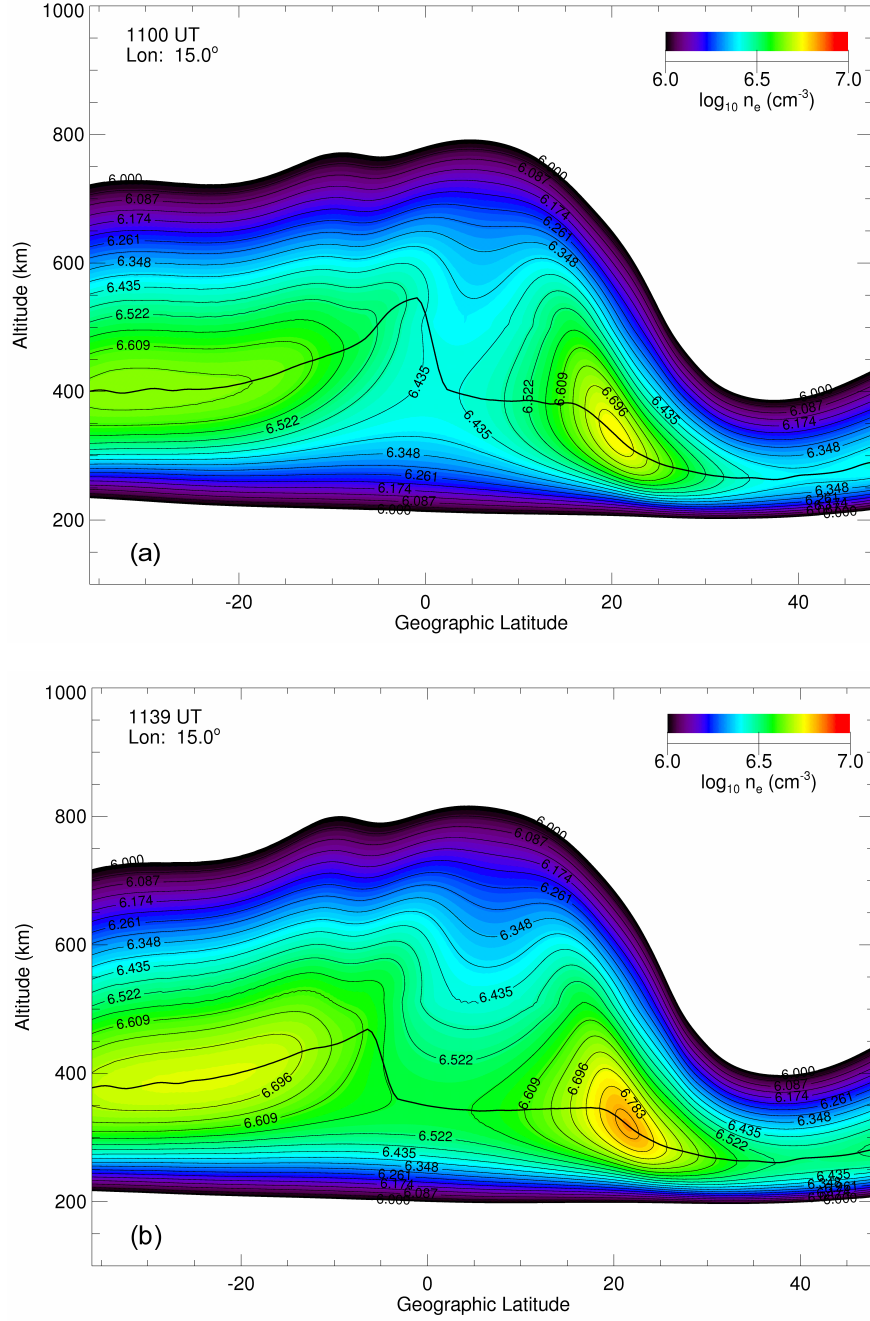
Figure 4.2. (a) Electron density (Log_{10} cm^{-3}) for 28 October, 2003 at 1100 UT/1200 L from modified SAMI2 using the FISM 60-second irradiance. The solid line shows the model height of the F_2 peak (H_mF_2). (b) The same at 1139 UT, 29 minutes after the flare peak X-ray intensity.

flare irradiance, and the solid line indicates the model run with the flare. It should be

noted that SAMI2 overestimates TEC, by an order of magnitude at some times during

the simulation. The reasons for this are not clear at present and the model authors are investigating *Huba*[private communication]. Despite this, H_mF_2 and N_mF_2 are in the range expected, and the ΔTEC observed due the flare is in line with the results from others [*Tsurutani et al.*, 2005]. In the top panel, N_mF_2 shows the greatest change in the mid-latitudes of the N. Hemisphere, followed by just north of the geographic Equator. The relative increase from $30° - 45°$ N averages $\sim 45\%$, while the relative increase on the north side of the geographic equator, to about $15°$, ranges from $20 - 35\%$. In the S. Hemisphere the change is a more modest, and constant, $10 - 12\%$ in the low and mid-latitudes. While ΔTEC is uniform in absolute terms, it is not in relative terms. In the southern mid-latitudes, the increase of 22 TECU equates to a 12.5% relative increase, while at the sub-solar point, around $13°$ S, the 27 TECU amounts to 15.3%. In contrast, the N. Hemisphere mid-latitudes, with a baseline of ~ 49 TECU rises by more than 30% with the flare.

The change in H_mF_2 is least in the mid-latitudes of both hemispheres, where it lowers by $10 - 15$ km in the S. Hemisphere and by $1 - 3$ km in the N. Hemisphere. The height lowers considerably more near the equator, however, this is somewhat misleading. It is likely that the area around the dip equator ($0°$ magnetic) displays a high altitude trough in electron density because of depletion from the *equatorial fountain* effect, which in turn causes the Appleton anomaly. During the daytime, an eastward electric field causes upward, $\mathbf{E} \times \mathbf{B}$ drift of the plasma along the dip equator. The plasma then diffuses along the magnetic field lines, descending under the influence of gravity to form the density maxima on either side of the equator.

This continuous upwelling of plasma depletes the region around the dip equator until it can fill again due to photoionization during the day. The strong enhancement of the shortest wavelengths by the flare disproportionately increases ionization at the lowest altitudes replenishing the depleted region faster than normal. So the larger decrease near the equator is certainly enhanced, but is not solely a result of the flare. This is borne out by later plots (not shown) which indicate a recovery of the H_mF_2 to a non-flare profile by 1300 UT.
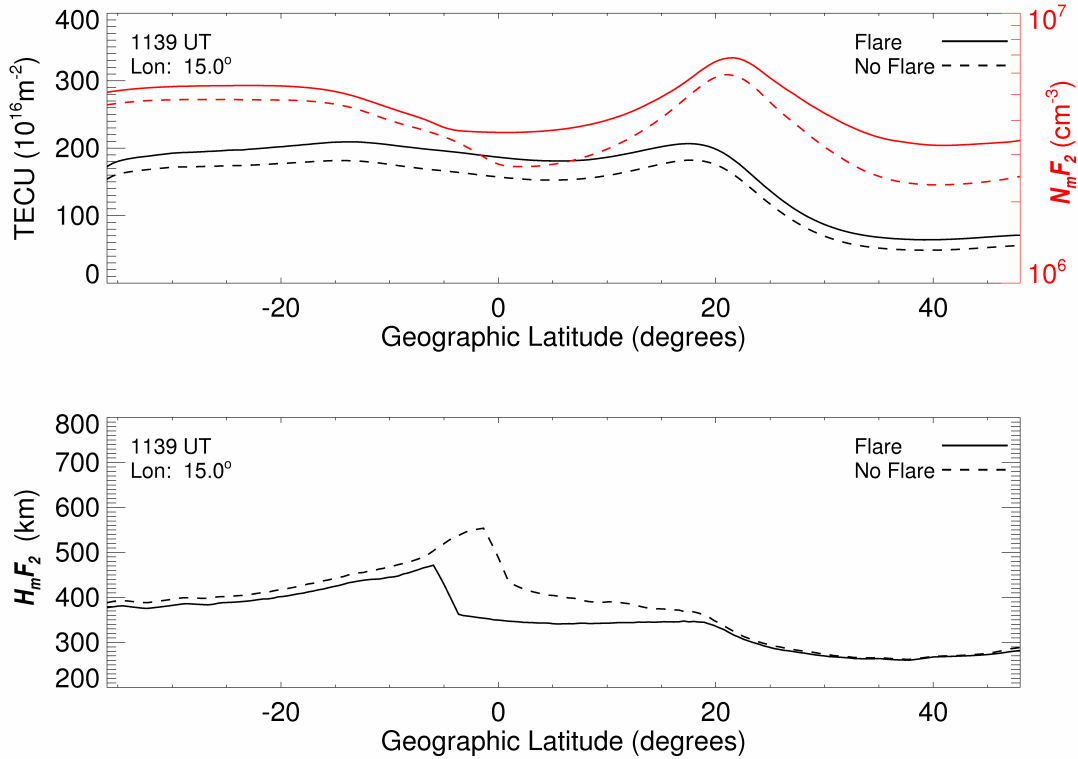
Figure 4.3. **Top** - Total electron content (TEC) 1×10^{16} m^{-2} in black, and the electron density in cm^{-3} at the F_2 peak (N_mF_2) in red, for 28 October, 2003 at 1139 UT. Dashed lines indicate no flare and solid lines indicate the flare run. **Bottom** - Height (km) of the electron density peak (H_mF_2) for the same model runs, date, and time.

The evolution of the flare over the next three hours is shown in Figure 4.4a - c, where only TEC and N_mF_2 are shown. TEC recovers fastest in the N. Hemisphere,

decreasing to less than a third of its peak increase by 1410 UT. In contrast, the S. Hemisphere decreases by a third. This trend continues for several more hours and by 1600 UT the flare TEC in the S. Hemisphere, especially near the sub-solar point, is still $15-20$ TECU above the non-flare level, while the N. Hemisphere is only 2 TECU above normal. Not surprising is the correlation between the $N_m F_2$ and TEC, since the greatest contribution to the modeled TEC is in the region of the F_2 peak. Between $22°$ and $30°$ N, both TEC and $N_m F_2$ approach the no-flare values more rapidly than at other latitudes. This is also due to the continued $\mathbf{E} \times \mathbf{B}$ drift and diffusion of plasma which, although enhanced by the flare, is not the dominant transport mechanism at these latitudes. The N. Hemisphere $N_m F_2$ peak also exhibits a slow northward drift due to the influence of the northward, meridional neutral wind. By 1700 UT (not shown) there is only a 5% difference between the flare and no-flare model runs.
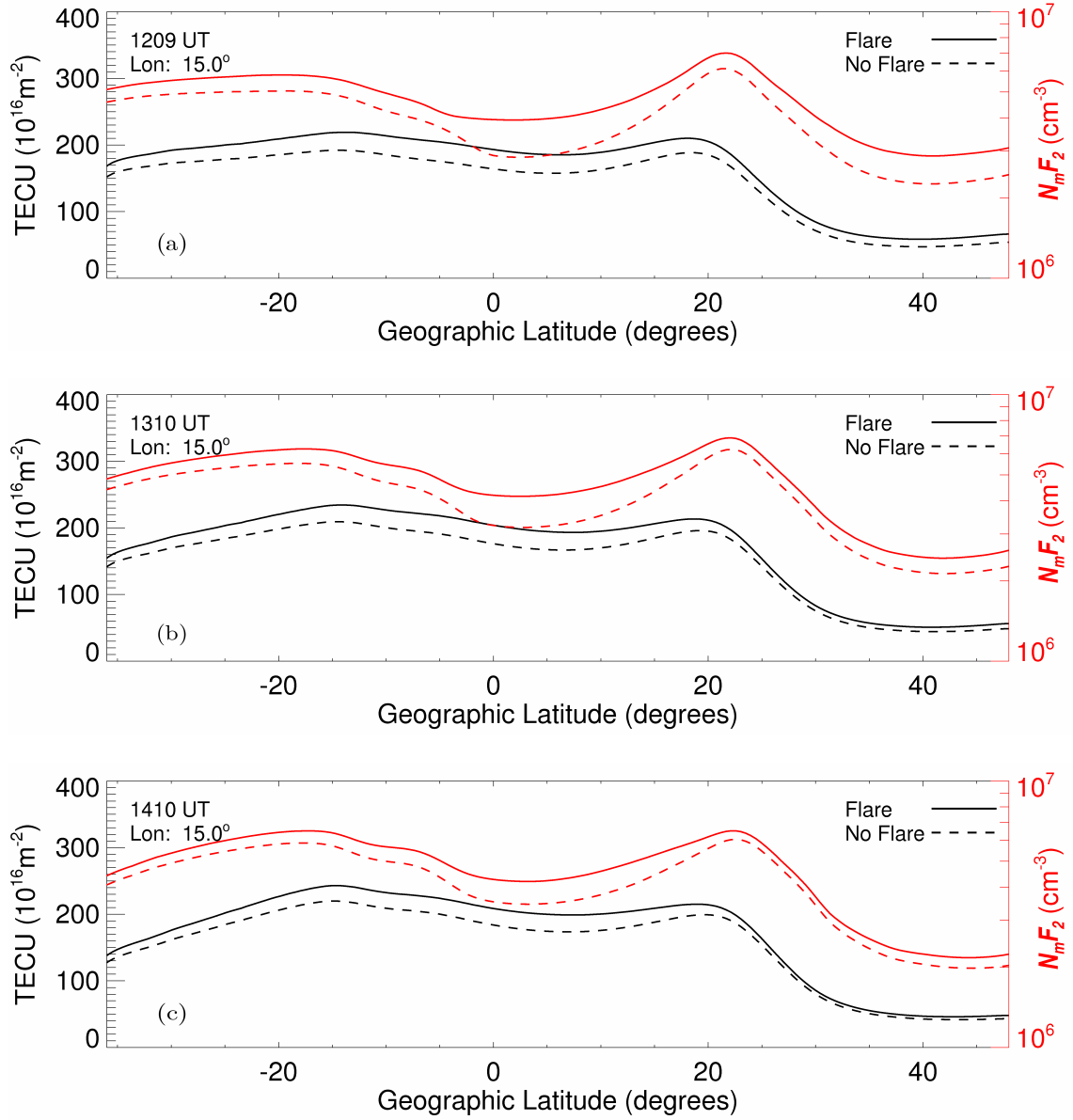
Figure 4.4. (a) Total electron content (TEC) in 1×10^{16} m^{-2} in black, and density in cm^{-3} at the F$_2$ peak (N_mF_2), in red for 28 October, 2003. Dashed lines indicate no flare, and solid lines indicate the flare run. (b) and (c) show the same at 1310 and 1410 UT, respectively.

4.2.2 Electron Density and Temperatures. Although it is not noticeable at F region heights, the electron density enhancement begins well before the flare irradiance reaches X-class levels. This happens at lower heights, chiefly below 120 km, due to the increase in X-ray and XUV flux from $0.05-1.8$ nm. Figure 4.5 illustrates this by plotting the first three bins of the *S&Q* 22-bin photon flux ($\#cm^{-2}$ s^{-1}). The dashed vertical line indicates the flare peak at 1110 UT. More than an hour before the flare peak, the flux in the $0.05-0.4$ nm bin flux increases by an order of magnitude, to $\sim 5 \times 10^5$, and then to 2.5×10^6 by 1030 UT. This increase is mirrored to a lesser extent, but in lock-step with the $0.05-0.4$ nm bin, in the $0.4-0.8$ nm bin. The trend of a diminished precursor flare continues as wavelengths increase, with the precursor becoming less noticeable in the $0.8-1.8$ nm bin. At longer wavelengths, or bins $4-22$ (not shown), only the main flare is significant.

The evolution of the electron density has a significant effect on T_e due to the neutral and ion cooling terms, Q_{en} and Q_{ei}, in equation 3.7. Figure 4.6 shows the ionosphere's response to the flare over 17 minutes, from $1105-1122$ UT. Figure 4.6a shows the ratio of n_e (flare/no flare) and Figure 4.6b shows the difference of electron temperature (flare - no flare), or ΔT_e. At 1100 UT (not shown) the first effects is an increase in the electron density below 120 km. From $100-120$ km the enhancement is around 20%, while below 100 km it varies, from 50–80% in the southern mid-latitudes to more than 200% elsewhere. At 1105 UT, shown in Figure 4.6, the changes are much more dramatic.
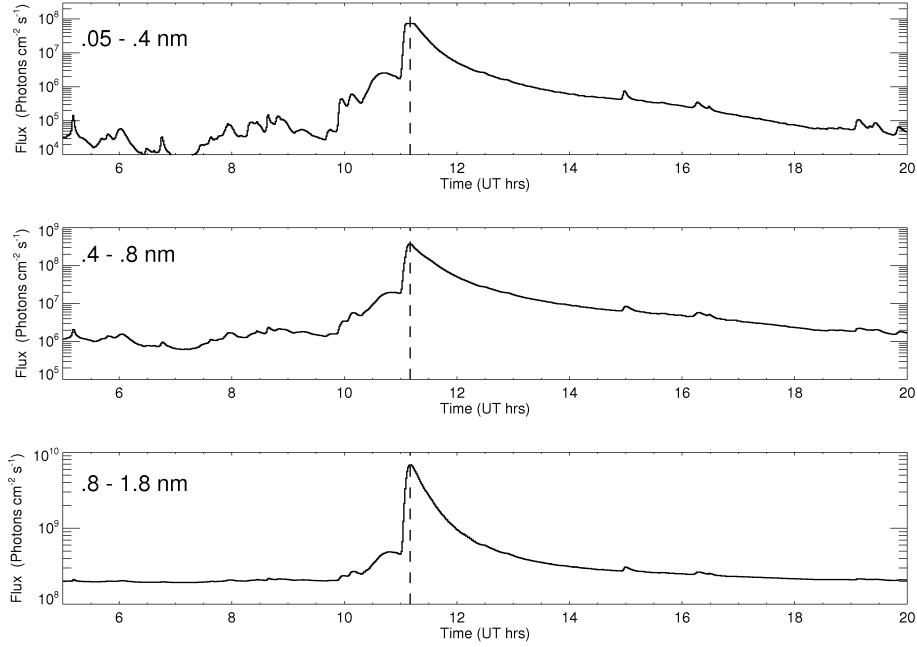
Figure 4.5.   Photon flux (photons cm^{-2} s^{-1}) for the three shortest wavelength bins for the 28 October, 2003 solar flare. The FISM model and GOES-12 0.05−0.4 nm and 0.1−0.8 nm flux are combined to yield irradiance in the 22-bin *Solomon and Qian* [2005] format. The dashed vertical lines indicate the peak of the flare as measure by GOES-12.

The increased flux prior to the flare peak increases the density at all altitudes up to 600 km, with the soft X-rays depositing their energy at low altitude, leading to increases of 200−800% below 120 km. An +80% maxima begins to appear from 23° S to 26° N at 175 km, and an equatorward-sloping trough in the contours appears from 200−300 km between 20−28° N. This trough coincides with the position of the N. Hemisphere n_e maximum and persists until around 1330 UT, at which point the only remaining maxima are above 0° and 40°. The two ridges at 0° and 38° N correspond to minima in the electron density as shown in Figure 4.2a; the former is underneath the equatorial inverted n_e trough while the latter coincides with the N. Hemisphere mid-latitude n_e trough. In the middle (1110 UT) panel the southern

63

low-latitude maximum reaches a mximum of 200% and has lifted slightly. This trend continues in the bottom panel (1122 UT) with a clearly defined maximum of 80%. The ridging above this point is also more pronounced with >10% values now reaching above 400 km. As this maximum lifts, to an altitude of 500 km by 1410 UT, it drifts northward and slowly decays, still being visble as a >20% enhancement over 0° at 1510 UT. This maximum appears to be due to XUV production of O^+ from a combination of direct photoionization and secondary impact ionization.

The 1-D ion density above 3° S shows that, between 1100 and 1110 UT, the O^+ density from 180−290 km increases substantially; by more than a order of magnitude between 190 and 220 km. The subsequent migration is caused by a combination of a meridional neutral wind that acts from south to north, and thus moves the plasma up the field lines, and, as the field lines become more nearly horizontal, an upward-directed $\mathbf{E} \times \mathbf{B}$ drift due to the eastward *equatorial electrojet* [*Schunk and Nagy*, 2000]. The plasma, initially formed by increased production of O^+, is lifted out of the collisional regime to an altitude where it can persist, allowing the parcel to be easily identified until around 1700 UT.

Figure 4.6b shows the response of T_e to the flare. As in Figure 4.6a, the response is seen well before the flare peak. T_e responds very quickly to changes in photoionization; in some respects the flare response is analogous to that seen at sunrise, where the large increase in T_e is very rapid, decaying as the electron density increases over 1−3 hours. The increase in photoionization causes the Q_{phe} term in equation 3.7 to outstrip the cooling and advection terms. This effect is first seen by

64
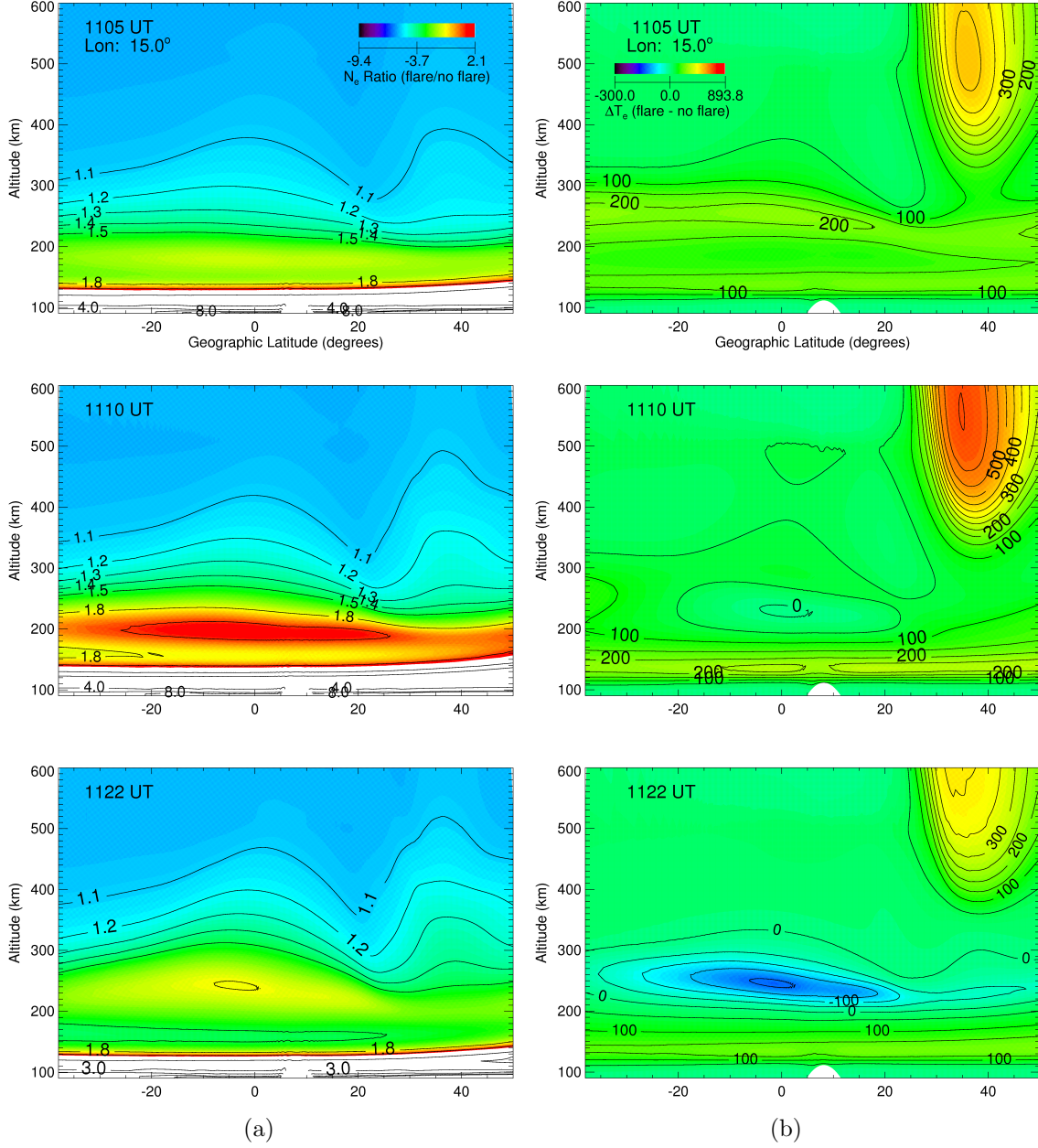
Figure 4.6.   Ratio of n_e and T_e difference for the flare and no flare model runs for the 28 October, 2003 flare. (a) shows the ratio of electron density, n_e, and (b) shows the difference in electron temperature, ΔT_e, between the flare and no flare runs.

1102 UT (not shown) as a broad increase in T_e throughout the model domain, elevated slightly between 130 and 250 km, as well as a maximum centered above 35° N at 500 km. By 1105 UT, the N. Hemisphere maximum is clearly defined as is a swath

of $\Delta T_e > 200$ K from 36° S to 19° N at 250 km. In the middle panel (1110 UT), the N. Hemisphere maximum has intensified, while the previous *broad swath* has eroded, replaced now by a layer of $\Delta T_e > 200$ K centered at 140 km. What is happening makes sense if the role of n_e and n_n are considered in our cooling terms.

The collisional heating terms, Q_{en} and Q_{ei} [*Schunk and Nagy*, 2000], from equation 3.7 are given by:

$$Q_{en} = \sum_n \frac{m_e n_e}{m_n} \nu_{en} 3k_B \left(T_n - T_e\right) \tag{4.1}$$

and,

$$Q_{ei} = \sum_i \frac{m_e n_e}{m_i} \nu_{ei} 3k_B \left(T_i - T_e\right) \tag{4.2}$$

where the subscript n and i indicate all species of neutrals and ions, respectively. The species-dependent collision frequencies are:

$$\nu_{en} \propto n_n \tag{4.3}$$

and,

$$\nu_{ei} \propto \frac{n_i}{A_i T_e^{3/2}} \tag{4.4}$$

where A_i is the ion molar mass. Therefore, Q_{en} is proportional to both n_e and n_n; whereas, Q_{ei} which dominates above $\sim$200 km, is proportional to $n_i \times n_e$, or $\sim n_e^2$ [*Schunk and Nagy*, 2000]. Below 200 km, n_n is many orders of magnitude greater

than n_e and effectively dominates Q_{en}. Also, T_n is not affected by an increase in T_e; therefore, as T_e gets larger, Q_{en} becomes more negative.

The net result of this is that, at altitudes below 200 km the deposition of SXR energy results in a large increase in n_e, but only a modest, ~ 250 K, increase in T_e due to the strong coupling with neutrals. This strong coupling explains why cooling is never observed below 200 km as it is at higher altitude. The neutral density is unaffected by the flare, and the increased SXR, drives both the higher electron density and electron temperature.

Above 200 km, T_e responds quickly to the higher Q_{phe}, however n_e takes longer to respond, continuing to increase past the flare peak. As the flare progresses to the peak and beyond, Q_{phe} decreases, while Q_{ei} increases, which it continues to do as long as n_e continues to increase.

At the flare peak, Q_{phe} is high across the domain; however, at low altitudes, n_e increases more rapidly than at higher altitudes. Due to the coupling to the neutrals, the initial peak in T_e is not followed by a net cooling. Between $200-300$ km, n_e increases rapidly (Figure 4.6a), and losses due to Q_{ei} quickly dominate Q_{phe}, which is still positive at this time owing to the slow decay of the flare (still X-class at 12UT).

The maximum centered above 35° N at 550 km follows a similar cycle, but on a longer timescale. Looking back at Figure 4.2a, the maximum ΔT_e occurs in an area of low n_e. This is partially due to the new *Smithtro and Solomon* photoelectron heating parameterization. As seen in Figure 3.8, the use of the new parameterization places

the transition height very near 500 km for periods of high solar activity (496 km for the flare). Although there was not a significant difference in electron volume heating rates between similar latitudes above the F_2 region, a strong S. Hemisphere bias was seen below 200 km, where the maximum increase was about 200% greater than that in the N. Hemisphere. Therefore, the cause for the asymmetric high altitude heating seems not to be differenct heating rates, but different electron densities.

Examining n_e and Q_{phe} along a field line show that, near 500 km, the electron density in the S. Hemisphere is more than an order of magnitude greater than in the N. Hemisphere, but the volume heating rate is only twice as much. A direct comparison between 35° S and 35° N revealed that at 500 km, the heating rate per electron (eV/s) is more than 280% greater in the N. Hemisphere. Having established the reason for the large temperature increase, the evolution is much the same as the region over 3° S at 250 km; however, it is much slower. The additional photoelectron heating (Q_{phe}) ceases at the same time as for the aforementioned region, but n_e is still very low and increasing slowly. This is eveident by the decrease in ΔT_e. The temperature continues to decrease, and by 1154 UT (not shown) a ΔT_e minimum has formed at ~ 450 km, above 35° N. T_e continues to drop and the area expands to fill the region once occupied by a positive ΔT_e by 1239 UT. The temperatures do not recover full until after 1500 UT.

The lack of a large T_e increase below 110 km is due to the fact that T_e and T_n are strongly coupled at low altitudes and MSIS-00, the neutral atmosphere model, does not respond to external forcing of the temperature. Also, the high neutral density

$(10^{11} - 10^{12}$ cm^{-3}) insures that any increase will be relatively short-lived due to the strong neutral coupling.

4.3   Mid-Latitude versus Low-Latitude

This section will compare and contrast the flare response at a low-latitude, 3° S, and mid-latitude, 35° N, location. These two location were chosen because they represent latitudes that exhibited the greatest changes in T_e and/or n_e due to the flare. Although the S. Hemisphere did show an increase in TEC, this was expected and doesn't warrant in-depth analysis. In contrast, at low-latitudes, it is the southern hemisphere which exhibited the strongest response to the flare. At the flare peak, the solar zenith angle at 3° S was 10.8° and at 35° N it was $\sim 48°$. As in the previous section, comparison of the flare and no-flare model runs illustrates, not only how the response varies from low to mid-latitudes, but also the magnitude of the changes.

Figure 4.7 plots the electron volume heating rate (eV cm^{-3} s^{-1}) at the flare peak, for flare and no-flare runs of SAMI2 at 3° S and 35° N. The solid lines indicate the heating rate with flare irradiance and the dashed lines indicate the run without. The responsiveness of the *Smithtro and Solomon* heating parameterization to the additional short-wavelength flux is visible by the increase of $2-3$ orders of magnitude near 100 km.

Figure 4.7a displays a discontinuity that results from using different equations (3.12 and 3.14) for the low and high altitude collision regimes. Rather than plotting the electron volume heating rate along a field line, the heating rates are plotted above

specific points. Therefore, they are the result of the heating rates from as many field lines as intersect a vertical line above the location. Since the transition point is at ~ 500 km, locations at low altitude near the equator sample field lines which are entirely within the collisional regime, and are calculated by using equation 3.14, until the transition point is reached. This transition is apparent by the sharply decreasing slope at 500 km. Above this altitude the sampled field lines reflect a combination of local heating and non-local transport. Using the original version of SAMI2 revealed the same discontinuity, although not at 3° S. The much lower transition point (about 280 km) causes the discontinuity to reveal itself closer to the geomagnetic equator than in the new version.

Figure 4.8 shows 1-D plots of ion production rate $(\text{cm}^{-3}\ \text{s}^{-1})$ at 3° S and 35° N, during the 28 October, 2003 flare. It bears repeating that these production rates include photoionization, DI, and secondary impact ionization. The results of the simulation using flare irradiance are shown as dashed lines, while solid lines indicate the model run without it. Again, the ionization by XUV radiation is implied by the very large increase in ion and electron production below 200 km. In Figure 4.8a, the increase in e^- production at 100 km is two orders of magnitude, driven mainly by the factor of 39 increase in N_2^+ production. Figure 4.8b shows a similar situation with N_2^+ leading production, where increased production of O^+ at 180 km explains the increase in electron density seen in Figure 4.6.

Photoionization and photoelectron ionization from the flare lead to large differences in electron density with altitude. Regardless of what causes the increase, it is
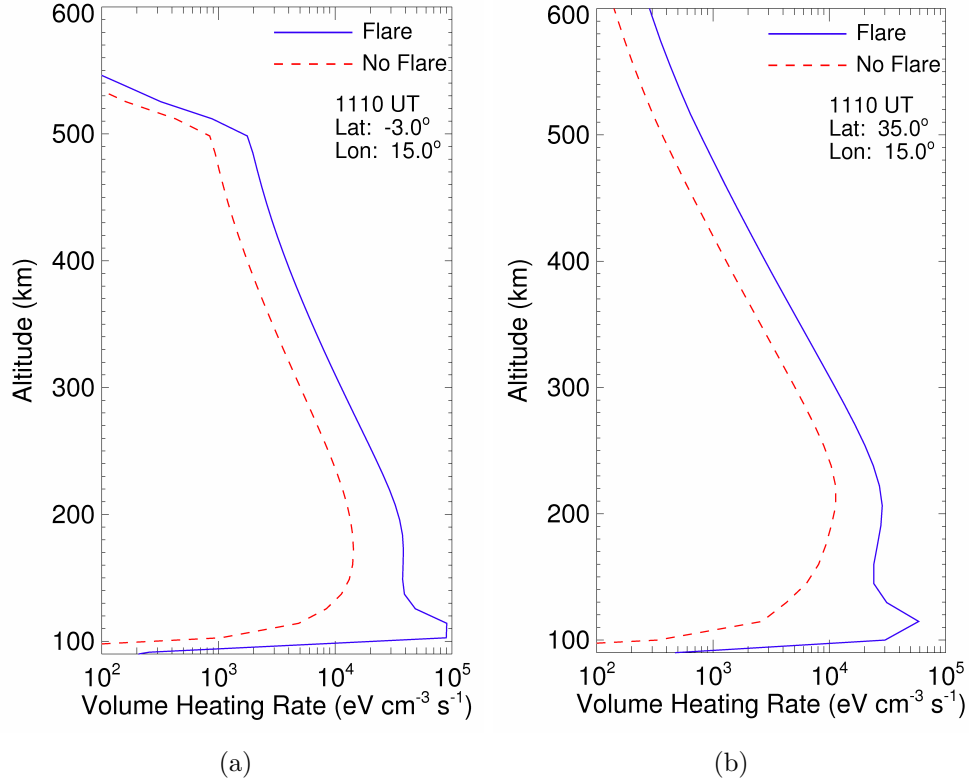
Figure 4.7.   Electron volume heating rate (eV cm^{-3} s^{-1}) at two different latitudes for flare and no-flare runs of SAMI2. The dashed line is the no-flare model run and the solid line includes the flare. (a) shows the volume heating rate at 3° S, (b) shows the rate at 35° N for comparison.

the altitude of formation that determines its longevity. Figure 4.9 shows contour plots

of the ratio (flare/no flare) of n_e with respect to altitude and time at 3° S and 35° N.

The flare peak is indicated by arrows above and below each plot. At both locations

the density begins to increase at altitudes below the F$_2$ peak at 1000 UT. This is

consistent with the M-class levels reached prior to the flare as seen in Figures 4.1 and

4.5. At the flare peak, Figures 4.9a and b show the result of increased ion production

in the form of up to an order of magnitude increase in electron density near 100 km.

The less-enhanced area between the peaks at 100 and ∼200 km corresponds to the

valley between the E and F regions, confirmed by analyzing a 1-D plot of electron
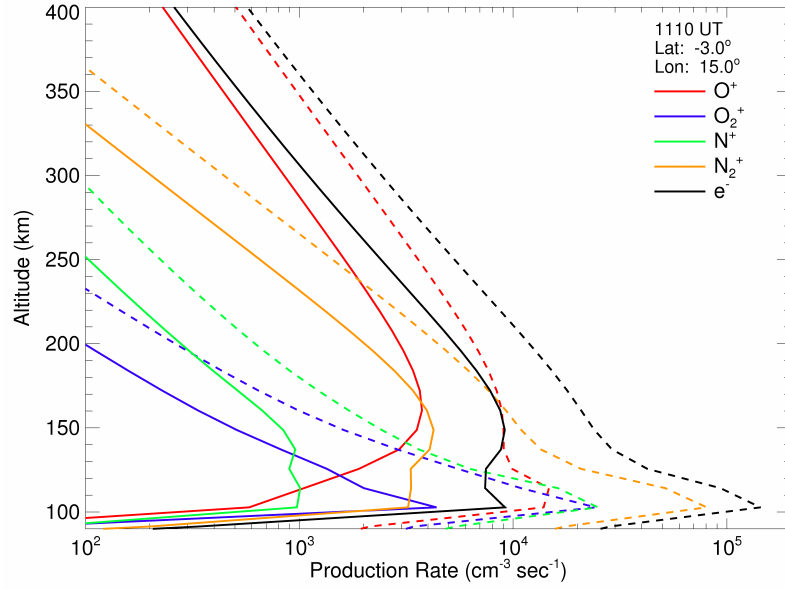
(a)
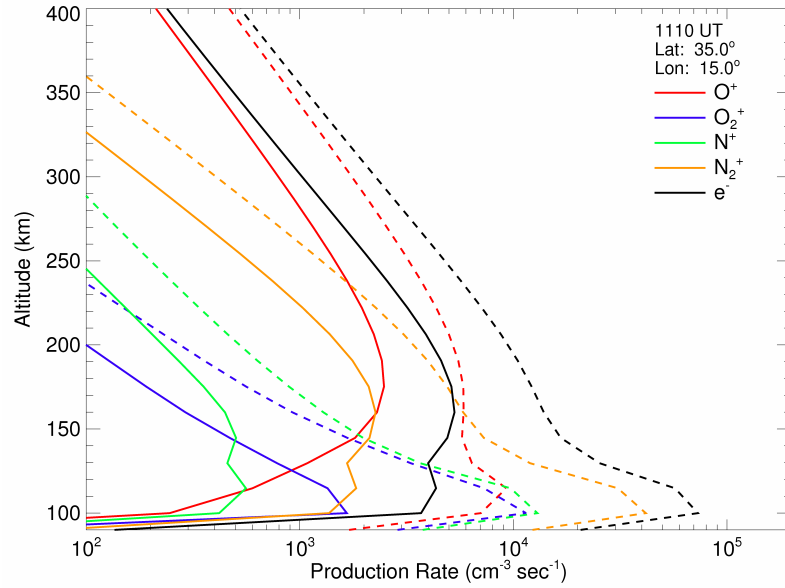
(b)

Figure 4.8. Ion production rate in cm^{-3} s^{-1}, for flare (dashed) and no-flare (solid) runs of SAMI2. The ion production rate includes photoionization, photoelectron impact ionization and dissociative ionization, but does not include production rate from chemistry. The rates are shown for 3° S in (a), and 35° N in (b) to illustrate the differences between low and mid-latitudes.

density (not shown). As time moves forward in Figure 4.9a, the 200 km density maximum, caused by increased O$^+$, diffuses upward as the neutral wind transports the

plasma along the magnetic field. This results in a northward drift until the plasma becomes affected by $\mathbf{E} \times \mathbf{B}$ drift at the dip equator. This was confirmed by running the model without any neutral winds, and with winds, but a reduced electric field. When the electric field was reduced, the movement of the low-latitude density maximum was not as pronounced, but was still discernible. Without the neutral winds, the winter anomaly fails to develop, resulting in symmetric density maxima in both hemispheres. The density increase due to the flare is almost symmetric with respect to the dip equator; there are slight differences due to the smaller zenith angle in the S. Hemisphere, and the differences associated with the neutral atmosphere model. The post-flare movement of the maximum without wind is upward, without latitudinal drift. The effect, of density increasing in altitude with time, is seen as far northward as 15° N (geographic), but diminishes rapidly between 10° and 15° and by 18° N it is gone entirely. In the S. Hemisphere it is clearly seen as far south as 20° S, or 27° S magnetic. This result may also be caused by enhanced EUV flux from the flare, whose slow decay is evident in the increased densities of 20−30% beyond 14 UT around 100 km.

In the N. Hemisphere mid-latitudes, Figure 4.9b, the increase is due more to changes in the plasma scale height caused by the increase in electron temperature. In the classical diffusive equilibrium equation [*Schunk and Nagy*, 2000]:

$$\frac{1}{n_i}\frac{\partial n_i}{\partial z} = -\frac{1}{H_p} - \frac{1}{T_p}\frac{\partial T_p}{\partial z} \tag{4.5}$$

73

where H_p is the plasma scale height, equal to $\frac{2k_B T_p}{m_i g}$, and T_p is the plasma temperature. It can be shown that in the limit of an isothermal ionosphere, the major ion and electron densities decrease exponentially with increasing altitude, at a rate determined by H_p. Thus, as the electron and ion temperatures increase, so does the plasma scale height, which in turn increases the slope of the density curves at high altitude. Finally, looking at how $N_m F_2$, $H_m F_2$, and TEC evolve with time over specific locations may shed some additional light on what's happening.

4.3.1 Temporal evolution of NmF2, HmF2, and TEC. $N_m F_2$, $H_m F_2$, and TEC were examined earlier in the chapter; however, looking at how they change in time may solidify some notions regarding the flare response to different regimes, e.g. collisional vs. transport-dominated. Figures 4.10 and 4.11 plot $N_m F_2$ and $H_m F_2$ in panel (a), and TEC in panel (b) at 3° S and 36° N, respectively. Dashed lines indicate the model run without flare irradiance and solid lines denote the run with flare irradiance. Again the flare peak is indicated by a vertical dashed line. Care must be taken when viewing these figures; although the ranges are consistent, the magnitudes are. This was done in order to fit all the data into the plot area.

The most obvious difference between the two locations is the decrease in $H_m F_2$, which is 191 km at 3° S versus only ~6 km at 35° N. In the case of the former, the maximum decrease lags the flare by 14 min, whereas there is virtually no lag at 35° N. This is a result of the very different pre-flare environments. In the S. Hemisphere the vertical extent of density greater than 3.09×10^6 cm^{-3} extends from $460-560$ km. In

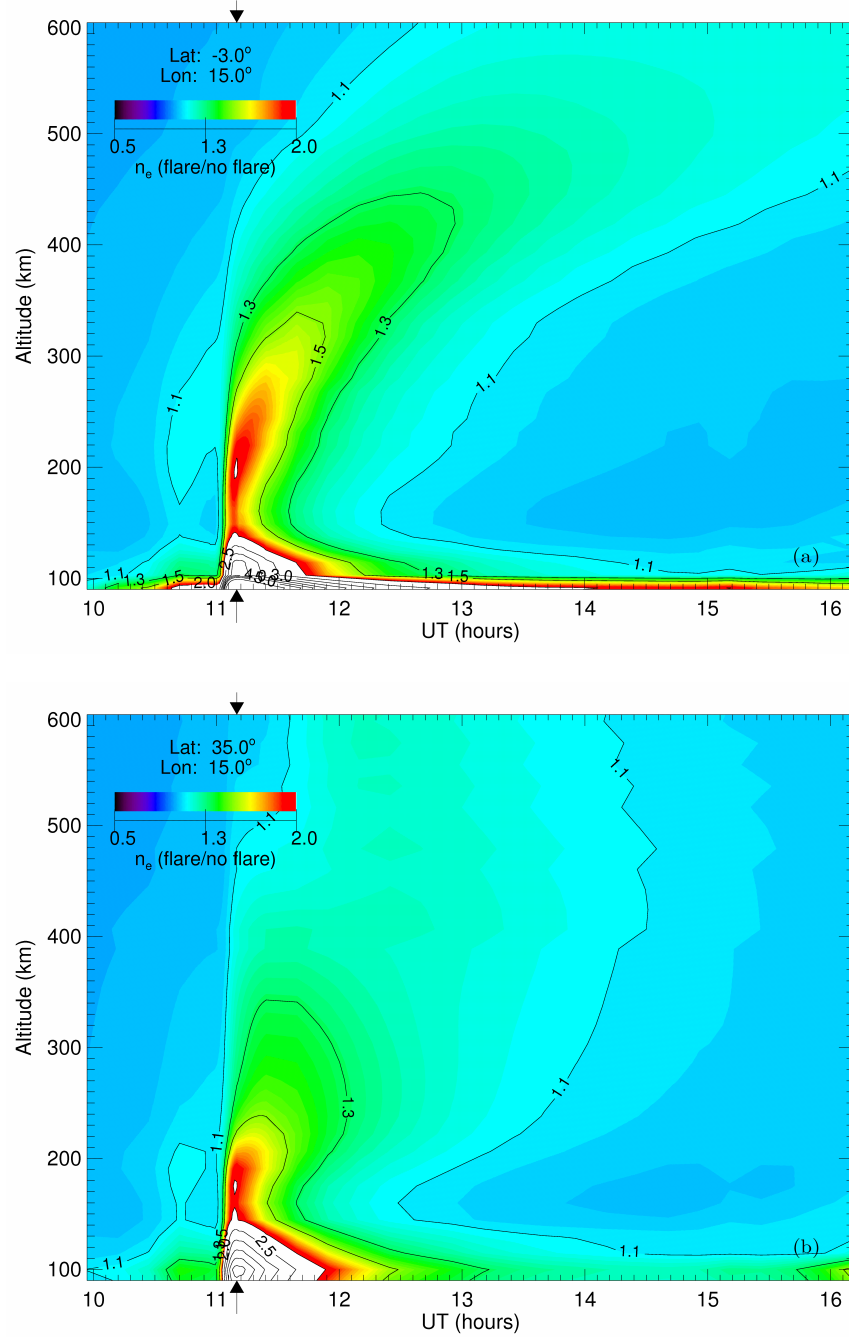Figure 4.9.   Contour plots of n_e ratio (flare/no flare) for modified SAMI2. The flare peak is marked by arrows at the top and bottom. (a) shows the volume heating rate at 3° S, (b) shows the rates at 35° N for comparison.

other words, it is broad and flat. Increased ionization of O^+ below the peak causes

the large drop in altitude of the peak, even though the relative increase in electron

density is only on the order of a few percent. Even as the H_mF_2 recovers, N_mF_2 slowly increases as two things happen: increased ionization continues due to the slow decay of the flare, and plasma is transported along field lines to higher altitudes. The broad vertical extent of O^+, seen in a 1-D plot of ion density, also accounts for the much greater increase in TEC seen in Figure 4.10b. That the plasma is in a region where recombination is slow accounts for the longevity of the increase in both TEC and N_mF_2.

In Figure 4.11a, N_mF_2 responds almost immediately to the flare when compared to the slower, but longer-lived, increase seen at 3° S. This difference is a result of the different mecahnisms involved, and the altitudes of H_mF_2 at the two latitudes. At 3° S, $\mathbf{E} \times \mathbf{B}$ drift of the plasma to heights where transport dominates and recombination is slow accounts for the longevity, and slow increase, of N_mF_2. At 35° N, the increase is due to direct photoionization from the flare, with transport playing a much smaller role. As such, N_mF_2, and the F_2 region as a whole, in the N. Hemisphere mid-latitudes is at an altitude where electron recombination occurs on a much faster time scale. This is evident in the much faster decay of N_mF_2 at 35° N to near the no-flare level when compared to 3° S. The dependence of TEC on N_mF_2, shown in Figure 4.10b and 4.11b, is such that the evolution of TEC mirrors that of N_mF_2.
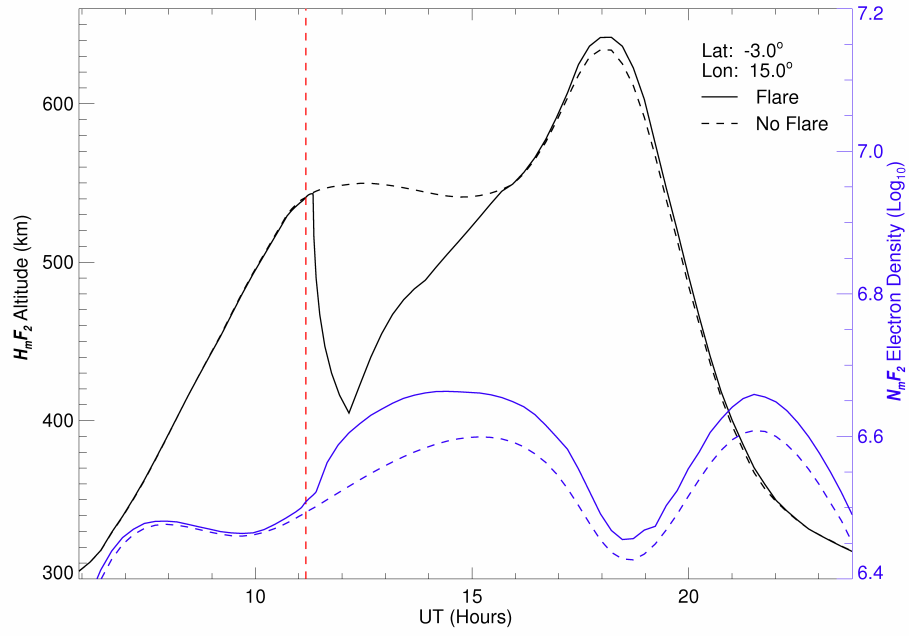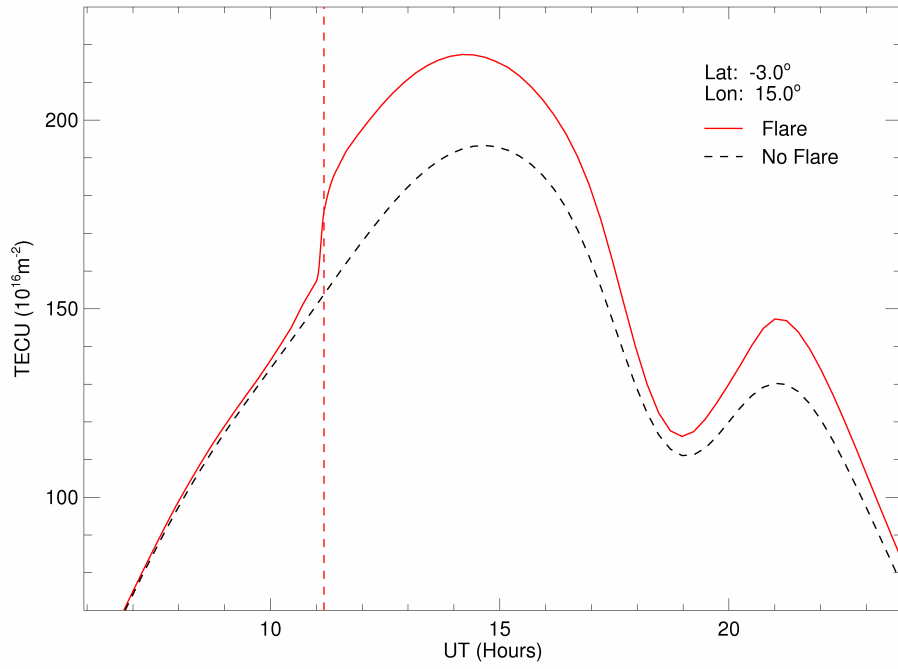
Figure 4.10. N_mF_2, H_mF_2, and TEC at 3° S for modified SAMI2 showing evolution with time for the solar flare of 28 October, 2003. The flare peak is marked by the vertical dashed line at 1110 UT. **(a)** plots N_mF_2 in cm^{-3} s^{-1} (blue lines) and H_mF_2 in km (black lines). **(b)** plots the total electron content (TEC) in TECU$=10^{16}$ m^{-2}. Solid lines indicate the flare run, dashed lines indicate the no-flare run.
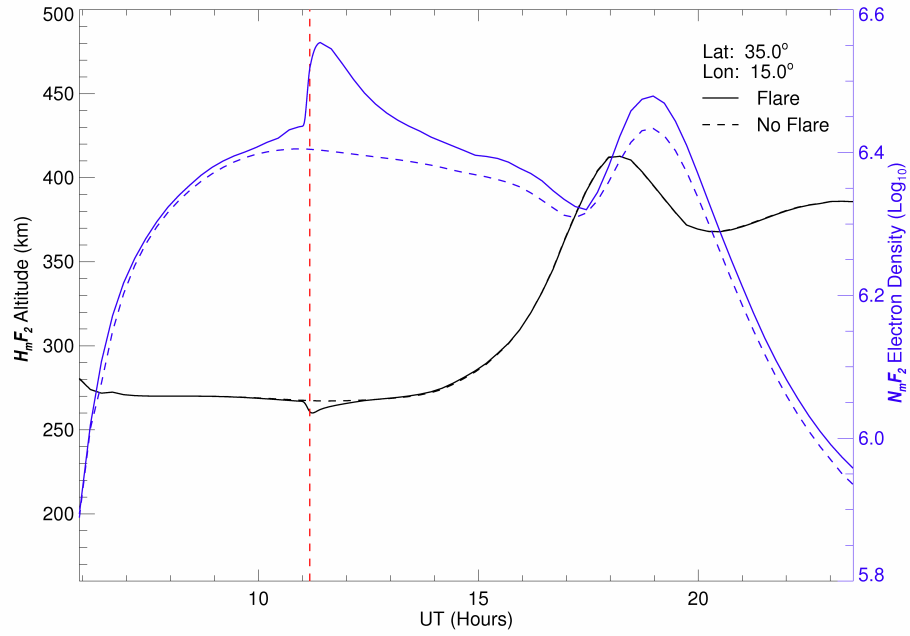
(a)
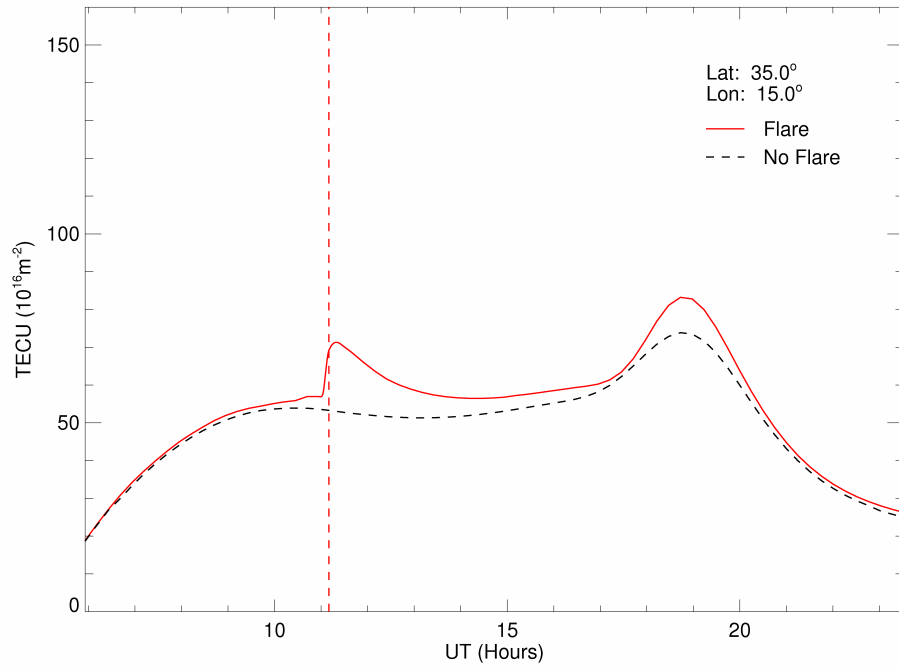
(b)

Figure 4.11. N_mF_2, H_mF_2, and TEC at 35° N for modified SAMI2 showing evolution with time for the solar flare of 28 October, 2003. The flare peak is marked by the vertical dashed line at 1110 UT. **(a)** plots N_mF_2 in cm^{-3} s^{-1} (blue lines) and H_mF_2 in km (black lines). **(b)** plots the total electron content (TEC) in TECU = 10^{16} m^2. Solid lines indicate the flare run, dashed lines indicate the no-flare run.

4.4 Comparison to other results

This section concludes with a brief comparison of the results to some of the previous work mentioned in Chapter I. In general, the results of the model compared well with what other researchers have found.

The up to $\sim$30 TECU increase found in this study is comparable to the maximum estimated by *Tsurutani et al.* [2005]. They measured a 25 TECU maximum at the subsolar point, based on TEC from GPS data. The Libreville, Gabon GPS station recorded a maximum increase of $\sim$30 TECU on two of the six tracked satellites. Located at 0° N/9° E, it was near the subsolar point, making it a good measurement of the actual increase. The results from SAMI2 indicate that, at least in the low-latitude region, that the long-lived increase in TEC is due to the combined effects of neutral winds, and $\mathbf{E} \times \mathbf{B}$ drift of plasma from lower altitudes.

This is validated by examining the variation of O^+ density with altitude. At 3° S/15° E the maximum increase in density compared to the no-flare run occurs at 230 km at the flare peak. This increase of nearly 100% is easily followed at subsequent times. By 1124 UT this maximum has increased in altitude and magnitude, exceeding the magnitude of the no-flare F_2 peak at $\sim$600 km. This explains the cause of the abrupt descent of $H_m F_2$ seen in Figure 4.10a.

Figure 4.12 shows the evolution of ΔT_e (flare - no-flare) with time and altitude for 3° S and 35° N. Figure 4.12b displays the large ΔT_e due to the combination of photoelectron heating and low density, which transitions to a net cooling as Q_{phe}

decreases as n_e increases. This is absent in Figure 4.12a due to the much higher electron density, by an order of magnitude, at this altitude. Both latitudes exhibit very similar low (200−300 km) altitude trends, although the cooling at 3° S is greater due to the higher density (see Figure 4.9) in a region where the cooling rate is still proportional to n_e^2. Near 150 km, the important collisions are with neutrals. T_e is coupled closely to the neutral temperature and, is cooled according to equation 4.1. This coupling also dampens the effect of the surge of high-energy photons deposited at this height. The weaker coupling at 500−600 km at 35° N explains the much larger ΔT_e, as T_e is able to respond freely to the influx of energy. This 2-D analysis of ΔT_e was also used by *Smithtro and Solomon* [2008].

Smithtro and Solomon [2008] also used the 28 October, 2003 flare to test the new photoelectron heating parameterization using a 1-D model for 40° N. The results from SAMI2 were very similar with the following differences observed: First, the flare-induced positive ΔT_e at 500 km is around 100 K higher; cooling of the region is less rapid, taking 30 minutes more in to reach $\Delta T_e = 0$; finally, cooling was less pronounced remaining around 100 K warmer than the 1-D model. The exact magnitude, and timing, of the temperature change is not as important as the fact that the change was observed at all. As shown earlier, the electron heating and cooling rates at this altitude vary as n_e^2.
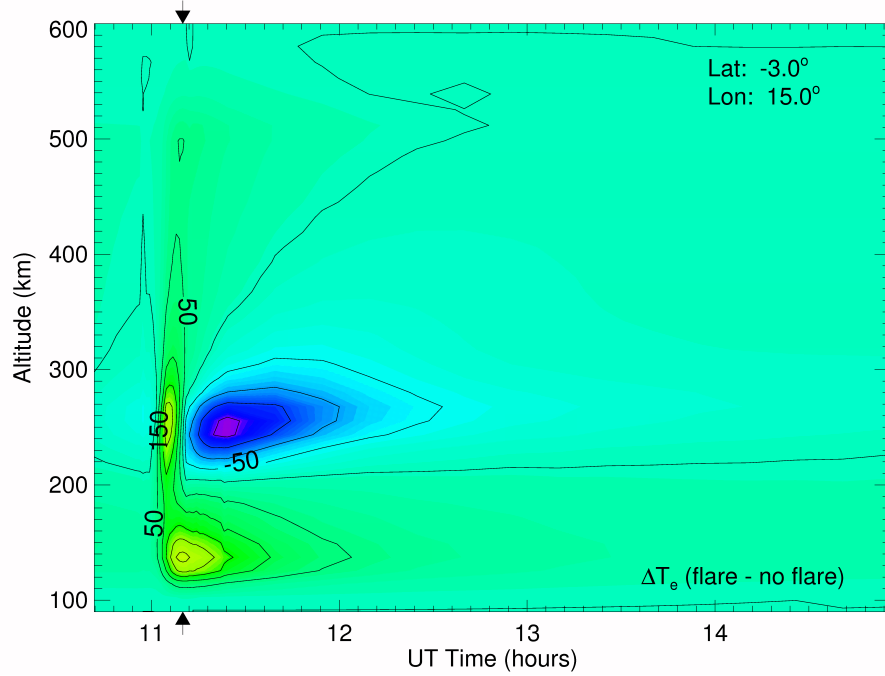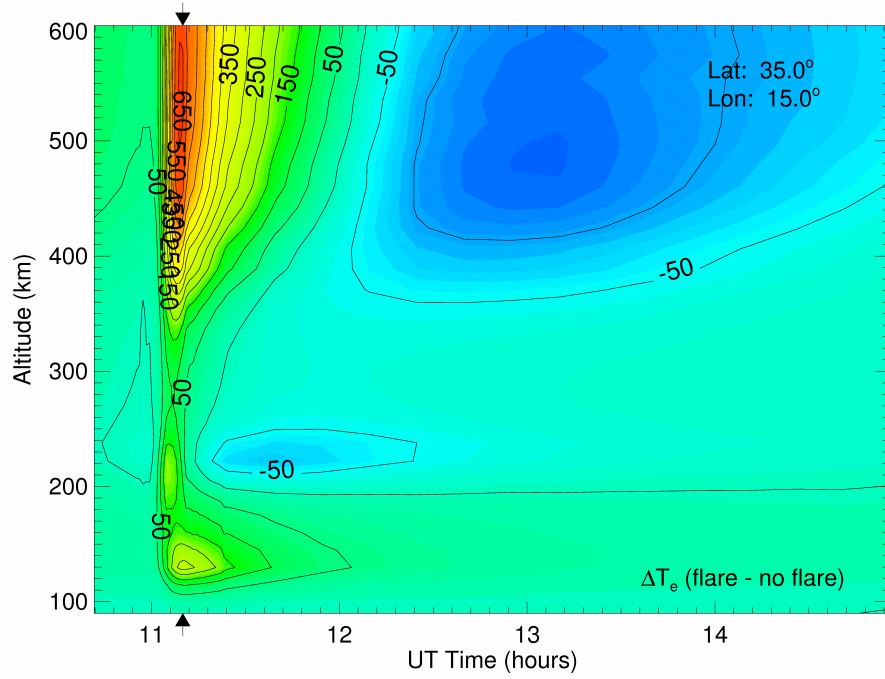
Figure 4.12. Temperature difference ($\Delta\mathrm{T}_e$ in Kelvin) between flare and no-flare runs of the modified SAMI2 model. The scenario is the X17 solar flare of the 28 October, 2003. **(a)** is for $3°$ S/$15°$ E and **(b)** is for $35°$ N/$15°$ E, from $10-14$ UT/$11-15$ L.

V. Conclusions and Suggestions for Future Work

THIS chapter presents the conclusions drawn from this research. It also explains the impact of the research to the United States Air Force and makes suggestions for future work in this area.

5.1 Summary of Research and Conclusions

The SAMI2 model presents a unique opportunity to researchers. It is one of a number of two-dimensional ionospheric models, which are complete enough to provide meaningful results, yet efficient enough to run on a laptop computer. It has also been designed to be easily upgradeable and can incorporate better models of variables such as the neutral winds and neutral atmosphere as they become available.

First and foremost, the research was successful. SAMI2, in its original configuration, is not capable of adequately modeling the ionospheric response to solar flares because of three key limitations. First, the input solar irradiance, based on the EUVAC model, lacks the temporal resolution needed to capture the evolution of the flare. Second, secondary ionization by photoelectrons, which are particularly sensitive to the enhanced SXR wavelengths from a flare, is not included. Finally, SAMI2 uses an older parameterization for photoelectron heating, which is unresponsive to the short-wavelength bias of the flare spectrum. These limitations were removed with the first being the addition of photoelectron ionization.

The impact of photoelectron ionization in the vicinity of the ionization peak for O^+, O_2^+, and N_2^+ has been known for many years [*Richards et al.*, 1994; *Woods et al.*,

2003]. At the production peak, the effect can be equally as important as direct photoionization [*Richards et al.*, 1994]. Photoelectron ionization was successfully added to SAMI2, and demonstrated that the model could generate an E region peak, in addition to an improved representation of the F_1 peak. This addition came as a result of incorporating the *Solomon and Qian* [2005] low-resolution irradiance method.

Second, the original photoelectron heating parameterization was not capable of responding to the enhanced flux from the flare. It was replaced with one capable of responding to the extreme variability of solar X-ray and XUV energy associated with flares. This new scheme not only allowed the model to generate more realistic *quiet sun* electron heating, but also to respond to flare irradiance with rapid non-uniform heating across the model grid.

Finally, the EUVAC flux model, which is based on a daily proxy and therefore unresponsive to the rapidly changing flux from a flare, was discarded in favor of a spectrum derived from the high-resolution FISM model. FISM was re-binned and combined with the GOES $0.04 - 0.5$ nm flux to generate a new *flare* irradiance according to the Solomon and Qian method. The model was then tested, modeling the ionospheric response to the X17.2 solar flare of 28 October, 2003.

The model was run with and without the high-cadence solar flux from the FISM model and GOES-12 solar X-ray flux, also sampled at one minute. Electron temperature and density variations across the model domain were compared to the model run without flare irradiance. Increases in total electron content (TEC), electron

density at various altitudes, including at the F_2 peak (N_mF_2) were observed, as were positive and negative changes in the electron temperature T_e. The simulation results were also compared to several studies and the new model was found to reproduce the observed increase in total electron content within 10%, especially near the subsolar point. The change in electron temperatures in the mid-latitudes are also within an order of magnitude of a 1-dimensional model. Although much work remains, the new version of SAMI2 will be a useful addition to the arsenal of models capable of predicting the ionospheric response to solar flares.

5.2   *Suggestions for Future Work*

The suggestions for future work can be summarized into two main categories: additional testing on flares and other events, and addressing anomalies and issues with the model which cropped up in testing. While this effort was successful, the new version remains relatively untested. The original plan for this project included a second flare event, also an X-class flare, however time did not permit adequate analysis of the second event. An updated non-flare version of SAMI2 was also used in a study of ionospheric conditions at Jicamarca, Peru, using incoherent scatter radar [*Hysell et al.*, 2007]. This version of SAMI2 was designed for parallel processing based on the message passing interface (MPI) standard. Although SAMI2's results were in very good agreement overall, a constant correction was applied to the photoelectron heating variable (Q_{phe}) in order to obtain the correct magnitude [*Huba*, 2007]. The version of SAMI2 from this paper generated lower temperatures, however the model

84

also generated anomalous patches of high temperature which were deemed not to be physically realistic. Huba was able to reproduce the instabilities using the open source SAMI2; however, the newer, parallelized version of the code used in the Jicamarca study did not exhibit the instability [*Huba*,private communication]. In the end, a comparison to [*Hysell et al.*, 2007] was abandoned, with the hope of eventually applying the changes from this paper to the parallel version of SAMI2. This leads to my first suggestion, which is to apply the improvements from this study to the MPI version of SAMI2. The open source SAMI2 is inferior to the latest version, which also incorporates a new version of the Horizontal Wind Model (HWM07) [*Hysell et al.*, 2007]. The fact that the newest version appears more stable is the main reason for this. Also a parallelized version would be ideal to take advantage of today's multi-core computers. Another troubling issue with the model is the tendency to overestimate TEC at high solar activity. Addressing this issue is also necessary before the model can be fully utilized. This issue was not uncovered early enough in the project to properly address, especially since the delta between the flare and no-flare runs was in good agreement with published results and the other data appeared valid. The problem may even be in the external routine used to calculate TEC from the model output.

In conclusion, the new, improved version of SAMI2 provides a new tool for studying the ionospheric response to solar flares. The low computational cost and easy modification of the code to add ion species, more chemistry, different wind or electric fields, etc. make it an attractive research tool. Now it can model the response

to solar flares. It is hoped that this additional capability will be used within the Department of Defense and United States Air Force to explore and better understand the complex reaction of the ionosphere to a flare event. Understanding the inter-hemispheric response to flares is a crucial step in predicting and mitigating the impact to our communications, navigations and space-borne assets.

Appendix A.   SAMI2 Input Parameters

THIS explains and lists the inputs to the modified version of SAMI2 that were used in modeling the response to the 28 October, 2003 solar flare. Additional parameters are listed and explained in the README file that accompanies the code package.

Table A.1.   SAMI2 Input parameters for 28 October 2003 solar flare simulation.

Variable	Value	
USEPE	.true.	Turns photoelectrons on and off
FLARE	.true.	Turns flare routine on and off
fejer	.true.	Uses Fejer and Scherliess electric field model or a sinusoidal model
rmin	90.0	Height of lowest the field line
rmax	7000.0	Height of highest the field line
nf	228	Number of field lines
nz	301	Number of grid point
f10p7	270.9	Daily $F_{10.7}$ index
fbar	138.7	81-day average of daily $F_{10.7}$
ap	21	Ap index value
nion2	7	Number of ions $(1-7)$
tvn0	1.	Factor for neutral wind
tvexb0	1.	$\mathbf{E} \times \mathbf{B}$ drift velocity
gams	3	Grid spacing along the field line
gamp	3	Spacing of the field lines
cqe	7.e-14	Constant for non-local photoelectron heating

USEPE is a logical parameter that turns on secondary ionization by photoelectrons. *FLARE* enables the solar flare subroutine which then reads the high-cadence irradiance data starting at 00 UT on the second day of the model run. The high cadence data output is started at a time given by *beginflr* and normal data output

cadence is resumed by *endflr*. Both *beginflr* and *endflr* are given in UT seconds + 86400, in order to account for running the model with a 24-hour burn-in period. This also requires the *day* variable to be set for the day prior to the flare day. *fejer* is also a logic variable that specifies use of the Fejer/Scherliess model of the electric field [*Scherliess and Fejer*, 1999] used to calculate $\mathbf{E} \times \mathbf{B}$ drift. Setting this to *.false.* forces SAMI2 to use a simpler sinusoidal drift model [*Huba et al.*, 2002]. *tvn0* is a multiplicative factor (0–1) for the neutral winds. Setting this variable equal to 0 turns off the neutral winds and 1 uses the unaltered (100%) winds from the HWM93 model. *tvexb0* does the same for the $\mathbf{E} \times \mathbf{B}$ drift velocity. *gams* sets the grid spacing along the magnetic field lines. The default setting is 3 and uses increases the spacing between points as altitude increases. A lower number makes the spacing more uniform. *gamp* does the same, but for the spacing between field lines at the magnetic equator. As altitude increases the spacing increases and a lower value makes the spacing more uniform. *cqe* is the correction factor C used in the photoelectron heating equation, equation 3.12. The normal value ranges from $3-8 \times 10^{-14}$.

Bibliography

Aschwanden, M. J. (2004), *Physics of the Solar Corona*, Praxis Publishing, Ltd.

Banks, P. M., and G. Kockarts (1973), *Aeronomy*, Academic Press, Inc.

Chamberlin, P. C. (2005), Flare irradiance spectral model (FISM): Daily component algorithms and results, Ph.D. thesis, Department of Aerospace Engineering Sciences, University of Colorado.

Chamberlin, P. C., T. N. Woods, and F. G. Eparvier (2007), Flare irradiance spectral model (FISM): Daily component algorithms and results, *Space Weather*, 5.

Foukal, P. V. (2004), *Solar Astrophysics*, Wiley-VCH Verlag GmbH & Co. KGaA.

Hedin, A. E. (1991), Revised global model of thermospheric winds using satellite and ground-based observations, *Journal of Geophysical Research*, 96.

Hinteregger, H. E., K. Fukui, and B. R. Gilson (1981), Observational, reference, and model data on solar EUV, from measurements on AE-E, *Geophysical Research Letters*, 8, 1147.

Huba, J. D. (2007), private communication.

Huba, J. D., G. Joyce, and J. A. Fedder (2000), Sami2 is another model of the ionosphere (SAMI2): A new low-latitude ionosphere model, *Journal of Geophysical Research*, *105*(A10), 23,035–23,053.

Huba, J. D., K. F. Dymond, G. Joyce, S. A. Budzien, S. E. Thonnard, J. A. Fedder, and R. P. McCoy (2002), Comparison of O^+ density from ARGOS LORAAS data analysis and SAMI2 model results, *Geophysical Research Letters*, *29*(7).

Huba, J. D., G. Joyce, and J. A. Fedder (2003), Study of mid-latitude ionospheric fluctuations observed at Millstone Hill, *Geophysical Research Letters*, *30*(18).

Huba, J. D., H. P. Warren, G. Joyce, X. Pi, B. Iijima, and C. Coker (2005), Global response of the low-latitude to midlatitude ionosphere due to the Bastille Day flare, *Geophysical Research Letters*, *32*(L15103).

Hysell, D. L., F. S. Rodrigues, J. L. Chau, and J. D. Huba (2007), Full profile incoherent scatter analysis at Jicamarca, submitted to Annales Geophysicae.

Lean, J. L., H. P. Warren, J. T. Mariska, and J. Bishop (2003), A new model of solar EUV irradiance variability 2. Comparisons with empirical models and observations and implications for space weather, *Journal of Geophysical Research*, *108*(A2).

Mariska, J. T., A. G. Emslie, and P. Li (1989), Numerical simulations of impulsively heated solar flares, *Astrophysics Journal*, *1067*(341).

Meier, R. R., et al. (2002), Ionospheric and dayglow responses to the radiative phase of the Bastille Day flare, *Geophysical Research Letters*, *29*(10).

Millward, G. H., R. J. Moffett, W. Quegan, and T. Fuller-Rowell (1996), A coupled thermospheric-ionospheric-plasmasphere model (CTIP, in *STEP: Handbook of Ionospheric Models*, edited by R. W. Schunk, Utah State University.

Parsons, A. M. (2006), Modeling E & F region ionospheric response to x-ray solar flares, Master's thesis, Department of Engineering Physics, Air Force Institute of Technology.

Picone, J. M., A. E. Hedin, and D. P. Drob (2002), NRLMSISE-00 empirical model of the atmosphere: Statistical comparisons and scientific issues, *Journal of Geophysical Research*, *107*(A12).

Richards, P. G., and D. G. Torr (1988), Ratios of photoelectron to EUV ionization rates for aeronomic studies, *Journal of Geophysical Research*, *94*(A5), 4060–4066.

Richards, P. G., J. A. Fennelly, and D. G. Torr (1994), EUVAC: A solar EUV flux model for aeronomic calculations, *Journal of Geophysical Research*, *99*(A10), 8981.

Scherliess, L., and B. G. Fejer (1999), Radar and satellite global equatorial F region vertical drift model, *Journal of Geophysical Research*, *104*.

Schunk, R. W., and A. F. Nagy (2000), *Ionospheres: Physics Plasma Physics and Chemistry*, Cambridge University Press.

Smithtro, C. G., and S. C. Solomon (2008), An improved parameterization of thermal electron hearing by photoelectrons, with application to an X17 flare, Submitted for publication to the Journal of Geophysical Research.

Smithtro, C. G., J. J. Sojka, T. Berkey, D. Thompson, and R. W. Schunk (2005), Anomalous *F* region response to moderate solar flares, *Radio Science*, *41*(RS5S03).

Solomon, S. C., and L. Qian (2005), Solar extreme-ultraviolet irradiance for general circulation models, *Journal of Geophysical Research*, *110*(A10), 10,306.

Sutton, E. K., J. M. Forbes, R. S. Nerem, and T. N. Woods (2006), Neutral density response to the solar flares of October and November, 2003, *Geophysical Research Letters*, *33*(L22101).

Swartz, W. E., and J. G. Nisbet (1972), Analytic expression for the energy-transfer rate from photoelectrons to thermal-electrons, *Journal of Geophysical Research*, *77*(31).

Tobiska, W. K. (2004), SOLAR2000 irradiance for climate change research, aeronomy, and space system engineering, *Advances in Space Research*, *34*, 1736.

Tsurutani, B. T., et al. (2005), The october 28, 2003 extreme EUV solar flare and resultant extreme ionospheric effects: Comparison to other halloween events and the Bastille Day event, *Geophysical Research Letters*, *32*(L03S09).

Warren, H. P., J. T. Mariska, and J. Lean (2001), A new model of solar EUV irradiance variability 1. Model formulation, *Journal of Geophysical Research*, *106*, 15,745.

Woods, T. N., S. M. Bailey, W. K. Peterson, S. C. Solomon, H. P. Warren, F. G. Eparvier, H. Garcia, C. W. Carlson, and J. P. McFadden (2003), Solar extreme ultraviolet variability of the X-class flare on 21 April 2002 and the terrestrial photoelectron response, *Space Weather*, *1*(1).

REPORT DOCUMENTATION PAGE

Form Approved
OMB No. 0704-0188

The public reporting burden for this collection of information is estimated to average 1 hour per response, including the time for reviewing instructions, searching existing data sources, gathering and maintaining the data needed, and completing and reviewing the collection of information. Send comments regarding this burden estimate or any other aspect of this collection of information, including suggestions for reducing the burden, to the Department of Defense, Executive Services and Communications Directorate (0704-0188). Respondents should be aware that notwithstanding any other provision of law, no person shall be subject to any penalty for failing to comply with a collection of information if it does not display a currently valid OMB control number.

PLEASE DO NOT RETURN YOUR FORM TO THE ABOVE ORGANIZATION.

1. REPORT DATE *(DD-MM-YYYY)*	2. REPORT TYPE	3. DATES COVERED *(From - To)*
27-03-2008	Master's Thesis	Aug 2007 - Mar2008

4. TITLE AND SUBTITLE	5a. CONTRACT NUMBER
Ionospheric Response to Solar Flares Using an Improved Version of SAMI2	5b. GRANT NUMBER
	5c. PROGRAM ELEMENT NUMBER

6. AUTHOR(S)	5d. PROJECT NUMBER
Reich III, Joseph, P., Capt, USAF	5e. TASK NUMBER
	5f. WORK UNIT NUMBER

7. PERFORMING ORGANIZATION NAME(S) AND ADDRESS(ES)	8. PERFORMING ORGANIZATION REPORT NUMBER
Air Force Institute of Technology Graduate School of Engineering and Management (AFIT/EN) 2950 Hobson Way, WPAFB OH 45433-7765	AFIT/GAP/ENP/08-M08

9. SPONSORING/MONITORING AGENCY NAME(S) AND ADDRESS(ES)	10. SPONSOR/MONITOR'S ACRONYM(S)
N/A INTENTIONALLY LEFT BLANK	11. SPONSOR/MONITOR'S REPORT NUMBER(S)

12. DISTRIBUTION/AVAILABILITY STATEMENT
APPROVED FOR PUBLIC RELEASE; DISTRIBUTION UNLIMITED

13. SUPPLEMENTARY NOTES

14. ABSTRACT
Solar flare-induced disturbances in the ionosphere can affect the propagation of electromagnetic waves, causing errors in GPS navigation, false radar echoes, and loss of HF radio communications. Accurately modeling the ionospheric response to flares is the first step in predicting, and eventually mitigating their effects. Sami2 is Another Model of the Ionosphere (SAMI2) is a 2-D ionospheric model, which, in its standard form, is ill-suited for studying solar flare effects because it lacks adequate temporal resolution of the solar irradiance, and does not account for photoelectron effects. These deficiencies are addressed, and the modified version is successfully used to model the response to the 28 October, 2003 X17.2 solar flare, along a 2-D hemispheric domain. The response to the flare varied significantly between the low and mid-latitudes, and between high and low altitudes.

15. SUBJECT TERMS
Ionospheric Models, Solar Flares, Ionosphere, Photoelectrons

16. SECURITY CLASSIFICATION OF:			17. LIMITATION OF ABSTRACT	18. NUMBER OF PAGES	19a. NAME OF RESPONSIBLE PERSON
a. REPORT	b. ABSTRACT	c. THIS PAGE			Christopher G. Smithtro, Lt Col, USAF, AFIT/ENP
U	U	U	UU	102	**19b. TELEPHONE NUMBER** *(Include area code)* 937-255-3636x4505, christopher.smithtro@afit.edu

Standard Form 298 (Rev. 8/98)
Prescribed by ANSI Std. Z39.18